MODELING OF POINT SPREAD FUNCTIONS FOR ASTRONOMICAL MULTIFIBER SPECTROGRAPHS

by

Parul Pandey

A thesis submitted to the faculty of
The University of Utah
in partial fulfillment of the requirements for the degree of

Master of Science

Department of Electrical and Computer Engineering

The University of Utah

December 2011

The University of Utah Graduate School

STATEMENT OF THESIS APPROVAL

This thesis of **Parul Pandey**

has been approved by the following supervisory committee members:

Adam Bolton, Chair	**09/30/2011** Date Approved
Neal Patwari, Co-chair	**10/03/2011** Date Approved
Tolga Tasdizen, Member	**09/30/2011** Date Approved

and by **Gianluca Lazzi**, Chair of the Department of **Electrical and Computer Engineering** and by Charles A. Wight, Dean of the Graduate School.

ABSTRACT

This thesis presents an improved method for reconstructing the spectra of astronomical objects from two-dimensional (2D) charge-coupled device (CCD) images. We address two issues, namely, estimation of calibration matrix for a CCD, and reconstruction of spectra of astronomical objects, which is referred to as extraction. In the first part of the thesis we estimate the elements of system calibration matrix by modeling the two-dimensional point-spread functions (PSF) in calibration images. Our PSF model is valid for arbitrarily complicated 2D point-spread functions, as compared to the state-of-art extraction methods which are valid only for class of separable PSFs. We present various models for PSFs and give a quantitative comparison between the models. In the second part of the thesis the system calibration matrix is used to extract the spectra of a particular type of calibration images called arc-images. We also address the issue of resolution and covariance in the extracted spectra, and present a method that establishes optimal properties in both these regards. We also compare quantitatively the performance of our extraction technique with the state-of-art extraction technique. The work presented in this thesis can be deployed for estimation of spectra of faint galaxies in presence of strong night-sky foregrounds.

To my advisor, Adam Bolton

CONTENTS

LIST OF FIGURES

LIST OF TABLES

ACKNOWLEDGEMENTS

When I first enrolled in University of Utah for the master's program I had no idea how amazing these two years of my life would be. I had very little idea about how I was going to spend these two years of my life. I am very grateful that I had the opportunity of working with my advisor, Adam Bolton. This section will not be sufficient to express my gratitude to my advisor. From my personal experience, Adam is the most ideal advisor one can expect to have. I am lucky to have him as my advisor and also to be his first graduate student. He was very helpful and patient in explaining every subtle aspect of my thesis. Apart from giving proper guidance, he encouraged me a lot in each and every aspect of my master's career. The most important of all are his great personal qualities that I picked up in the course of time. In spite of being brilliant at what he does, he is humble and respectful to everyone. I hope to incorporate these qualities in me and continue to strive for the best. I would also like to thank my parents for always being there for me and listening patiently about the problems I faced in my thesis. They supported me in spite of having no idea about my work. I also want to thank my friends, Deepika, Divya and Piyush, who with their idiosyncrasies made these two years worthwhile.

CHAPTER 1

INTRODUCTION

Spectroscopy is the technique of obtaining and studying the spectra of celestial bodies, from which their composition and motions can be determined. Spectrum is the variation of energy in the light per cm^2 per unit time with particular wavelength. The quantity, energy in the light per cm^2 per unit time at a particular wavelength is termed *specific flux*. The spectra are studied for certain features to determine the chemical composition of galaxies. The use of optical fibers provides us an advantage of recording the spectra of multiple astronomical objects simultaneously hence saving cost and time. Calibration forms an important step in the estimation of the spectrum of an astronomical object. This thesis explores the area of calibration in greater detail and introduces a novel technique to perform calibration. The images used in this thesis are a part of Sloan Digital Sky Survey-III (SDSS-III) database [1]. This chapter explains the hardware which is used to record the images, motivation of our thesis and contribution of our thesis to the area of astronomy. [2] [3]

1.1 Hardware

Figure 1.1 shows a schematic representation of the telescope and spectrograph used to capture the 2D spectrum images. It shows a telescope (obj.2) which is pointed towards the night-sky and receives light from multiple astronomical objects *simultaneously*. In our observation system there are a total of 1000 optical fibers [1] (obj.5). The light from each optical fiber passes through an arrangement which consists of collimator mirror, dichroic beam-splitter and diffraction grating (obj.6). The light from each optical fiber passes through the collimator mirror, which focusses the light into parallel beam. The light then passes to the beam-splitter which divides the light on the basis of wavelength range.

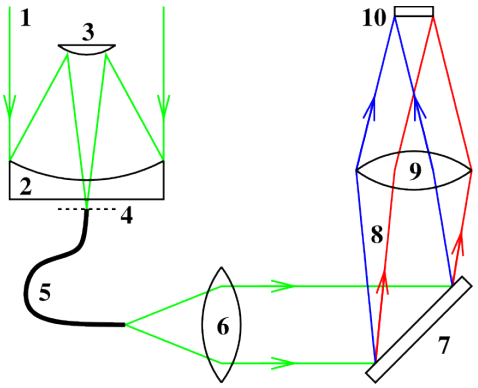

Figure 1.1: Schematic representation of telescope and spectrograph. courtesy: Prof. Adam Bolton, The University of Utah (unpublished)

One part is from wavelength range 5000 to 10000 Angstroms ($\mathring{A}$) called the red range and the other part is from 3600 to 6500 $\mathring{A}$ called the blue range. The light in each wavelength range now passes through the diffraction grating (obj.7). The diffraction grating separates the light in each range into its wavelength components. There are four cameras named *r1*, *b1*, *r2* and *b2* which capture light from the grating and record on a CCD detector. Camera *r1* receives light from the first 500 fibers and camera *r2* receives light from the remaining 500 fibers in the red range. Similarly, camera *b1* receives light from first the 500 fibers and camera *b2* receives light from the remaining 500 fibers in the blue range. The fibers, the spectrograph and the detector are so aligned that the wavelength direction corresponds to one axis of the two-dimensional CCD array which are shown as rows in our case. The other axis (columns) corresponds to positions of different fibers. Fig 1.2 shows a fiber bundle. Each fiber receives light from an astronomical object and passes it to the beam splitter. The beam splitter divides the light into two wavelength ranges. The red wavelength range is transmitted and the blue range is reflected. There are 25 such fiber bundles with 20 fibers in each bundle.

We also need bookkeeping to keep track of which fiber belongs to which astronomical object. Each blue and red light now passes through a diffraction grating which splits it into separate wavelength components. The CCD detector is aligned with the diffraction grating and the beam splitter in such a way that the one axis (rows) corresponds to different wavelength components and the other axis (columns)

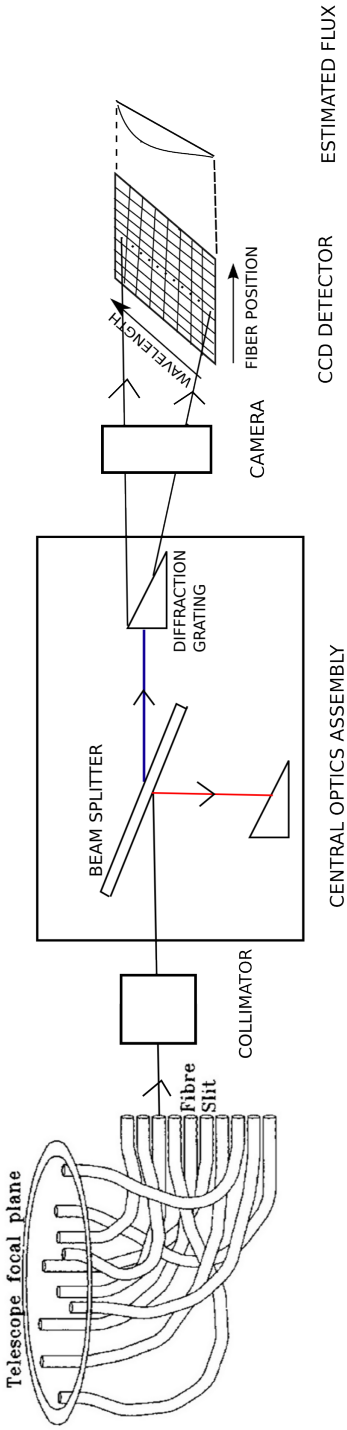

Figure 1.2: Schematic representation of recording of light on a CCD from a fiber slit

corresponds to position of fiber in the fiber slit. The data value at any pixel position in the CCD frame is called "counts." We assume a linear CCD detector in which the intensity of light captured by the CCD at a particular pixel is directly proportional to counts generated in that pixel.

1.1.1 Point Spread Function

After passing through the diffraction grating, light from an optical fiber separates into its wavelength components. The camera captures the image of fiber core emitting light at a particular wavelength. This image convolves with the optics of camera. The resulting image is pixelized by the CCD detector and is recorded. The recorded 2D image is called the Point Spread Function (PSF). Due to various optical aberrations like spherical aberration, astigmatism and coma in the camera, the recorded image is distorted [4]. The shape of this image varies across the CCD field of view. Fig. 1.3 shows the representation of a 2D PSF in an arc frame. The first image in the figure shows the arc frame where each white blob is the PSF. The second figure zooms in one series of blobs in an arc frame. These are 20 PSFs each belonging to a fiber of the bundle. The next figure is obtained by zooming in on one 2D PSF. It has a peak value (indicated by red) at the center and it decreases spatially on either side from the center.

1.1.2 Representation of Calibration Images

Calibration is the description of the way in which any set of astronomical and environmental stimuli translate into the responses of the digital detectors. [5]. We consider two types of calibration images, namely, arc-image and flat-field images. Figure 1.4 shows one such calibration image called as arc-image ("Arc"). Each illuminated blob represents a 2D PSF formed from a fiber at a particular wavelength. Each row represents PSFs at the same wavelength. In other words, a particular row is an indication of a particular wavelength. PSFs from fibers in a bundle appear together. Since the PSFs are formed by light at different wavelengths which are separated from each other, the PSFs are formed at rows which are also well separated from each other. Due to the separation there will not be any cross-talk between

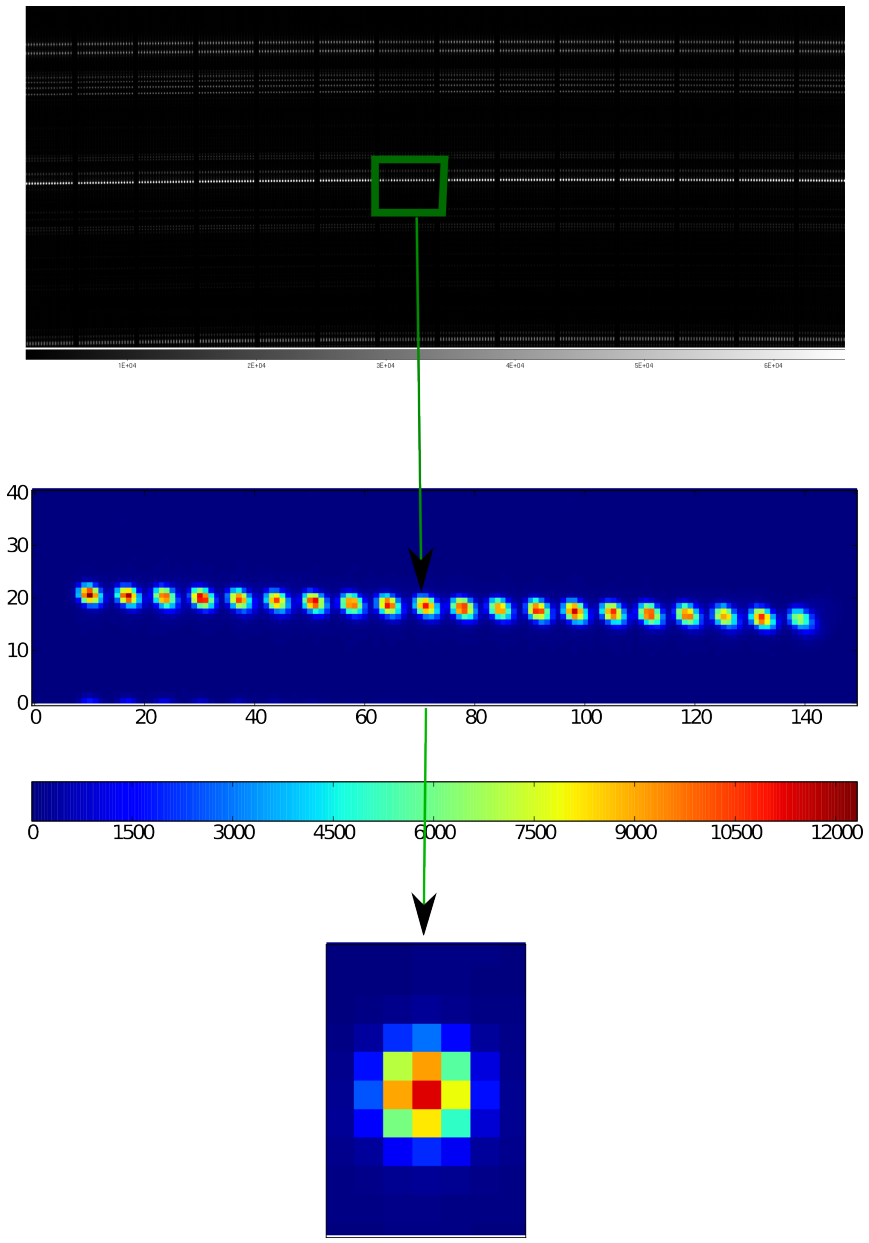

Figure 1.3: Representation of 2D PSF in a arc-frame

PSFs centered at separate rows (wavelength). As a result, we can determine the shape parameters for the PSF as a function of wavelength and fiber number. This image is used to determine wavelength solution which gives the wavelength value as a function of row number. This helps to know in which row the light of a particular wavelength falls. Fig. 1.5 shows CCD image called as Flat-images ("Flat"). These images are created by lamps which emit light at all the wavelengths recorded by the

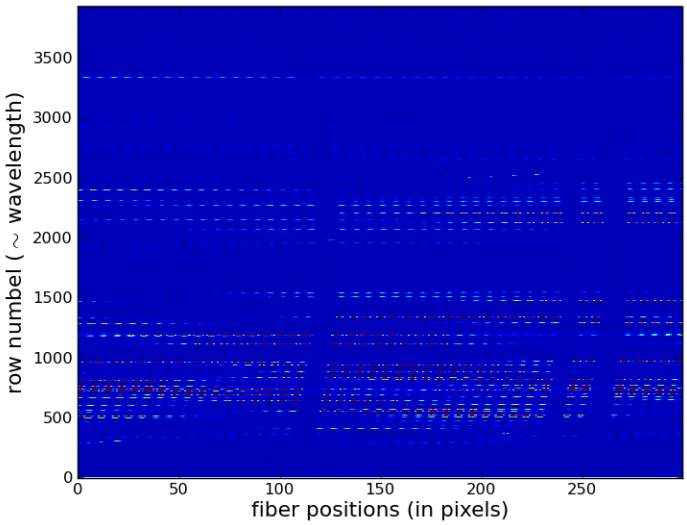

Figure 1.4: A section of arc image

CCD instead of few discrete wavelengths like the arc-frames. As a result a PSF is formed for all wavelengths (rows). Due to overlapping of PSFs in adjacent rows we do not see individual PSFs as arc-images but a continuous white line. These images are used to find the "trace" positions, which are the pixel positions of each fiber in the x direction for each row. It is also used to estimate relative fiber-to-fiber throughput at each pixel. The current SDSS standard assumes the PSF to have Gaussian shape and stores the shape parameters for these values in the database. The wavelength solution, fiber-to-fiber throughput are also stored in SDSS database. We used these values as the initial parameters in our simulations and optimized them further based on our new models.

1.1.3 Extraction

The spectrum of an astronomical object is defined as the variation of specific flux as a function of wavelength. Flux or intensity is defined as the energy in the light per cm^2, per second per unit wavelength. The optical fibers record the spectrum of different astronomical object in a two-dimensional CCD frame. Extraction is the process of estimating the one-dimensional spectrum one per fiber, from the two-dimensional CCD frame. It involves estimating the flux at different wavelengths where each wavelength occupies a distinct row of the CCD.

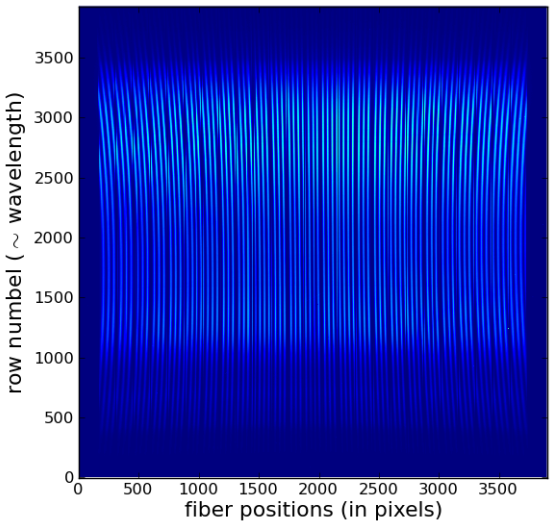

Figure 1.5: A section of flat image

1.1.4 Sky Subtraction

Typically, the spectrum of an astronomical object which is recorded has the spectrum of the night-sky superimposed on it. The sky acts as a foreground on the actual spectrum and contributes to the noise in the spectrum. Out of the 1000 optical fibers in a telescope, few fibers are not pointed towards any astronomical object and only record the spectrum of the night-sky. These fibers are used to estimate the spectrum of the night-sky. To get the actual spectrum of the target object we have to subtract the spectrum of sky from its estimated spectra which is obtained from CCD images. The accuracy with which sky contribution can be estimated determines the accuracy with which spectrum of the astronomical object can be estimated [6].

1.1.5 Scattered Light Correction

In Fig 1.2 we see that before being recorded by the detector, light from an optical fiber passes through a central optics assembly. Due to imperfections in the optics in this assembly some light from optical fibers is scattered [7]. This scattered light is not recorded on the row at which it should be recorded depending on its wavelength value. It can be recorded in any row. Due to scattering of light we see counts even at bundle gaps where we do not have any optical fiber and the count value should ideally be zero. Also, the scattered light is superimposed on the light from optical

fibers which causes the counts to increase in pixels where light from optical fiber falls. This scattered light can be seen as a smooth background added to the actual pixel counts. It is seen over the entire CCD frame and not just any particular region.

1.2 Motivation

The SDSS-III has recently initiated the Baryon Oscillation Spectroscopic Survey (BOSS) [8] which aims at targeting faint, distant galaxies with lower signal-to-noise ratio in comparison to the galaxies targeted by SDSS-I and II. The spectrum of the night sky which is superimposed on these galaxies however remains the same for all the galaxies irrespective of their distance from earth. Hence, our challenge is to extract the spectrum of faint galaxies in the presence of strong sky spectrum. The presence of sky errors in the estimated spectra of targeted object will make it noisy and reduce its quality. The sky spectrum which contributes to the noise remains the same for all surveys. Even after subtraction of sky spectrum from the spectrum of object we may observe sky residuals in the object spectrum. This makes the spectrum of low signal to noise ratio noisier in comparison to spectrum of galaxies with high signal to noise ratio. It will also make the detection of subtle features in the spectrum difficult. Hence, our aim is to remove our sky-subtraction residuals significantly in comparison to previous surveys. Although there have been attempts to partially remove the residual sky-subtraction residuals in the SDSS spectra [9][10], these are not sufficient in case of the faint galaxies which are being targeted by BOSS. Hence, we need to improve our calibrations to estimate the sky spectrum accurately and its projection into the frame of the 2D CCD image. This thesis presents a novel technique for calibration of 2D digital images which aims to improve the quality of estimation and subtraction of sky spectra.

1.3 Related Work

The state-of-art technique in SDSS is called the *optimal extraction* technique [11]. This technique fits a profile to the fiber profile in each row and the estimated amplitude is termed specific flux of the fiber in that row. This technique was implemented in many other forms in [12, 13, 14, 15, 16, 17, 18] [19] [20]. One of the

old spectrum extraction techniques is the boxcar-aperture summing technique. This technique defines flux at a given wavelength by summing all counts in the range of pixels occupied by a fiber at that wavelength. These methods and their shortcomings are discussed in detail in Chapter 2.

1.4 Contribution

This thesis presents a novel technique to construct the calibration matrix for a CCD detector. The calibration matrix is used to extract the spectrum of astronomical objects from two-dimensional CCD images or frames. The three main contributions of the thesis are:

1. Introducing three models for 2D PSF: Circular Gaussian, Gauss-Hermite and Modified Gauss Hermite model.

2. Introducing Lorentzian profile to model the wing component of the 2D PSF.

3. Presenting a technique to solve the problem associated with deconvolution of 2D CCD data.

We also present a quantitative performance analysis of various models that we have used. We also compare our model with the existing technique in SDSS and give a quantitative performance analysis of the two techniques.

1.5 Thesis Overview

The rest of the thesis is organized in four chapters and each chapter explains the research undertaken in achieving the contributions. Chapter 2 discusses briefly the currently implemented extraction techniques and their shortcomings. Chapter 3 explains the various models used for 2D PSF and compare the performance of these models. We also present a model for the wing component of the PSF. Chapter 4 talks about the extraction process and explains the problems witnessed during its implementation. It also discusses the method used to overcome them. Chapter 5 provides the summary of the results that we have achieved and explains the future areas of research which can be undertaken. Throughout the thesis we will denote vectors in lowercase bold-face type ($\mathbf{f}$) and matrices in uppercase bold-face type ($\mathbf{A}$).

CHAPTER 2

BACKGROUND

This chapter introduces the standard extraction techniques which have been implemented in various astronomical surveys. The first section of this chapter introduces Boxcar Extraction technique which is one of the most basic extraction techniques. The second section of the chapter includes the *optimal extraction* technique which is currently implemented to extract flux from 2D CCD images. The third section includes various challenges faced by any extraction technique and the inability of the existing extraction algorithms to overcome them. Finally, we discuss the model we have developed for our novel extraction technique.

2.1 Boxcar Extraction

This is one of the most basic and oldest extraction techniques. The flux from an optical fiber at a particular row is distributed in a profile on the CCD detector. To estimate this flux we make a box (aperture) around each fiber. Fig. 2.1 shows two black lines enclosing the fiber image. This box is bounded by midpoints between the two adjacent fiber profiles. Fig. 2.2 is obtained by zooming on one of the rows of Fig. 2.1. We estimate the flux value of a fiber in this row by summing the pixels enclosed by the box. This is done for all the rows of the fiber. This process is then repeated for all fibers of the CCD. This method is also referred to as tramline extraction [21]. The flux from all the contributing pixels j in profile i, for wavelength bin λ is given as

$$f = \sum_{j(i)} d_{j,\lambda} \tag{2.1}$$

where $d_{j,\lambda}$ is the count value at wavelength λ and pixel j.

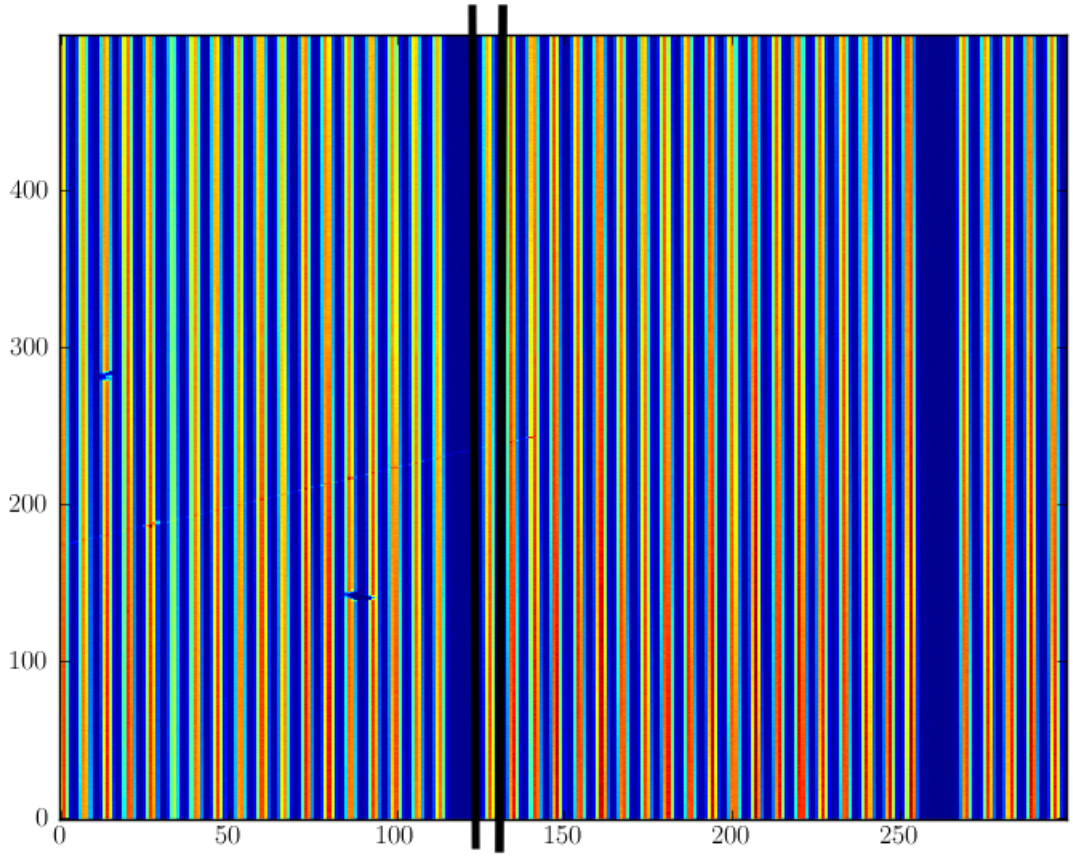

Figure 2.1: A section of flat-field image

This is one the fastest methods of extraction, although this method suffers from significant disadvantages. Since it gives equal weight to all pixels in the summation regardless of the flux level of the fiber profile in a given pixel, it propagates the maximum CCD readout-noise into the final extraction. Also, if the flux level is very low, then the contribution of readout-noise from outer pixels, which are surrounding the peak value as seen in Fig. 2.2, in a profile become significant and can even dominate flux errors [21].

2.2 Optimal Extraction

Optimal Extraction [11] is the state-of-art extraction technique implemented in SDSS-I and II. This method is more accurate than boxcar extraction. The flux

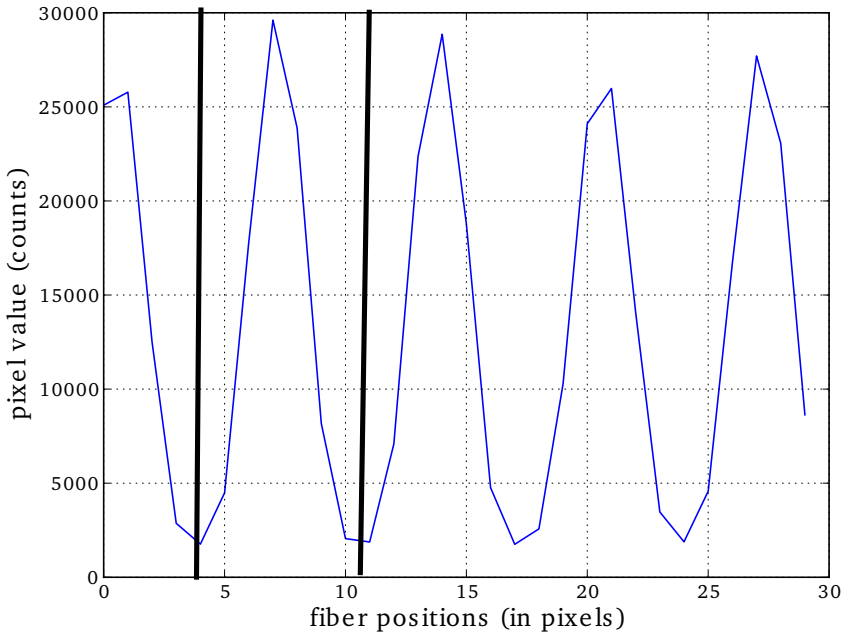

Figure 2.2: Cross-sectional profile across one bundle of a CCD

from every fiber in a wavelength bin (row) is distributed in a profile on a detector. The shape and extent of this profile depends on the detector [22]. In the current implementation of this method a Gaussian function is chosen to model each profile. To estimate the parameters (width and centroid) of the Gaussian function we use flat-field calibration images, which are discussed earlier in Section 1.1.2. This image is chosen because it is constructed by using lamps which emit light in the entire wavelength which is recorded by the CCD. Hence we can estimate profile shape parameters at all the wavelengths recorded by the CCD. We fit every profile in a row of a fiber bundle to a Gaussian function to estimate the parameters of the profile. The estimated parameters are used to create a profile for each fiber in every row. Each profile is hereafter normalized. This normalized profile tells us the distribution of count values on the CCD when a unit of flux at a particular wavelength falls on the CCD. A normalized spatial profile for fiber k at a particular wavelength is defined as a function of the CCD pixel i along the x-axis:

$$\sum_i \phi_{ik} = 1 \tag{2.2}$$

where ϕ_{ik} is the value of profile of fiber k at pixel i and f_k is the flux in fiber k

The model value for pixel i is given as,

$$M_i = \sum_k \phi_{ik} f_k \tag{2.3}$$

Given p_i and n_i be the count value and an the estimate of the statistical error at each pixel, we wish to estimate the f_k, which is the flux in each fiber. This is achieved by the χ^2 minimization of the residual R.

$$\chi^2 = \sum_i \frac{(D_i - M_i)^2}{n_i^2}, \tag{2.4}$$

and on setting $\frac{\partial \chi^2}{\partial f_k} = 0$ and substituting for M_i we find,

$$\sum_k f_k \sum_t \frac{\phi_{ji}\phi_{ki}}{n_i^2} = \sum_i \frac{\phi_{ji} D_i}{n_i^2} \tag{2.5}$$

where ϕ_{ji} is the normalized profile of fiber j at pixel i Letting

$$c_{kj} = \sum_i \frac{\phi_{ki}\phi_{ji}}{n_i^2} \tag{2.6}$$

and

$$b_j = \sum_i \frac{\phi_{ji} D_i}{n_i^2} \tag{2.7}$$

we find

$$\sum_k f_k c_{kj} = b_j \tag{2.8}$$

On solving coupled equation (2.8) we can get the value of flux f_k in each fiber.

The optimal extraction method allows for masking of cosmic rays. The pixels which are affected by cosmic rays have the value of inverse of n_i as zero. Boxcar extraction technique gives equal weight to all pixels and hence does not provide any protection from cosmic rays.

The optimal extraction technique suffers from various shortcomings. As we have discussed earlier the light at a wavelength for a fiber forms a 2D image (I) called the Point Spread Function. The optimal extraction technique estimates the flux in each row (wavelength bin) of the PSF independently of the other rows. It assumes that the 2D PSF *I(x,y)* is a separable function of x and y [5].

$$I(x, y) = I_x(x)I_y(y) \tag{2.9}$$

This assumption does not hold good for all the PSFs in the image. In fact, as we go from the center of the CCD to the edges, the shape of the PSF changes and is no longer a separable function of x and y. Our new extraction technique aims to model PSFs of all shapes across the CCD.

2.3 Challenges for an Extraction Algorithm

This section discusses the various challenges which are faced by an extraction algorithm.

2.3.1 Fiber-to-Fiber Cross-talk

The flux from a fiber in every wavelength bin (row) is distributed in a profile on a detector. This profile occupies a set of pixels. If the fibers are placed very close to each other, the profiles overlap with one another [23]. In case of SDSS, every fiber bundle has 20 fibers which are placed very close to each other. This results in overlap of profiles of adjacent fibers and this phenomenon is called cross-talk. Since the fiber bundles are well separated from each other, we do not observe any significant cross-talk between fibers of different bundles. The magnitude of the overlap depends on three factors: the spectrum separation, the width of the profile and relative intensity of each spectrum. The smaller the spectrum separation and the larger the width of the profile the greater the overlap. The SDSS optical system is constructed such that we can observe around 1000 different celestial objects together. To reduce the cross-talk the fiber-to-fiber separation can be increased. If the number of fibers is decreased, to increase the fiber-to-fiber spacing we would need multiple observations to record the same number of astronomical objects. This leads to increase in operational costs. Hence there is a trade-off between costs and fiber-to-fiber spacing. Fig. 2.3 shows a row across a CCD frame, showing two fiber bundles. Fig. 2.4 is obtained by zooming across one of the fiber bundles. We can see that the counts do not go to zero between two fibers. It is difficult to determine to which fiber profile these counts belong. The count between fibers in Fig. 2.4 is around the range of 2500 and the maximum

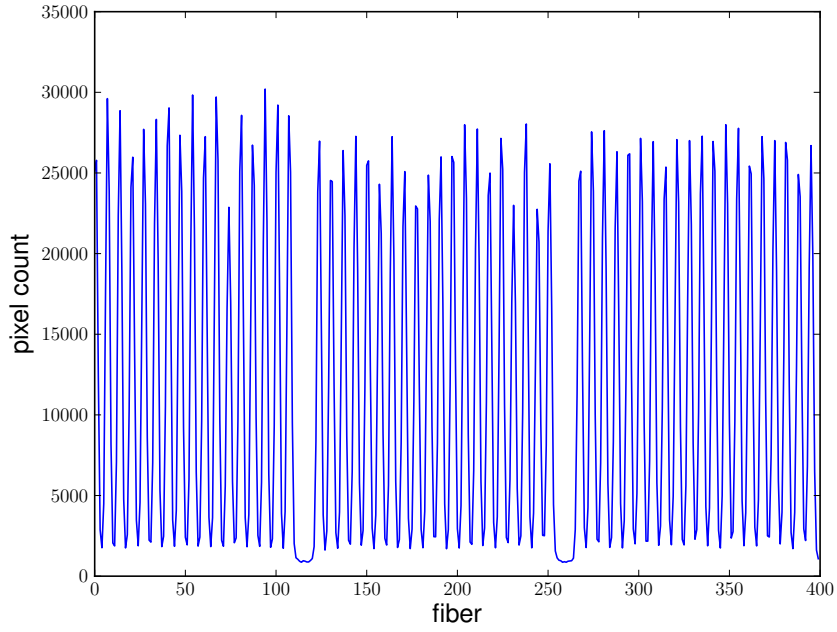

Figure 2.3: Cross-sectional profile across a CCD frame

count value is 25000. This shows that around 10% of the count values are affected by cross-talk. This number is significant and we need extraction algorithms which can correct for cross-talk. Optimal extraction technique provides correction for cross-talk, whereas Boxcar Extraction does not.

2.3.2 Blending

Blending is overlap of PSFs of a fiber formed at different wavelengths. A PSF which is formed by light from a fiber at a particular wavelength forms a 2D image on the CCD. Each 2D image occupies more than one row on the CCD and is centered at the row corresponding to its wavelength. Each PSF overlaps with PSFs of different wavelengths surrounding it. These PSFs are centered at different rows. This overlapping between PSFs in the wavelength or y-direction is called blending. Fig. 2.5 shows an arc frame which has PSFs centred at different rows. Fig. 2.6 shows a flat frame which is constructed by lamps which emit light at all wavelengths recorded by the CCD. Hence, PSFs are formed at all rows. Due to blending of PSFs in adjacent rows we see continuous white lines in Fig. 2.6. Similarly, an astronomical object also emits light in a continuous range of wavelengths. Hence the PSF will be formed at

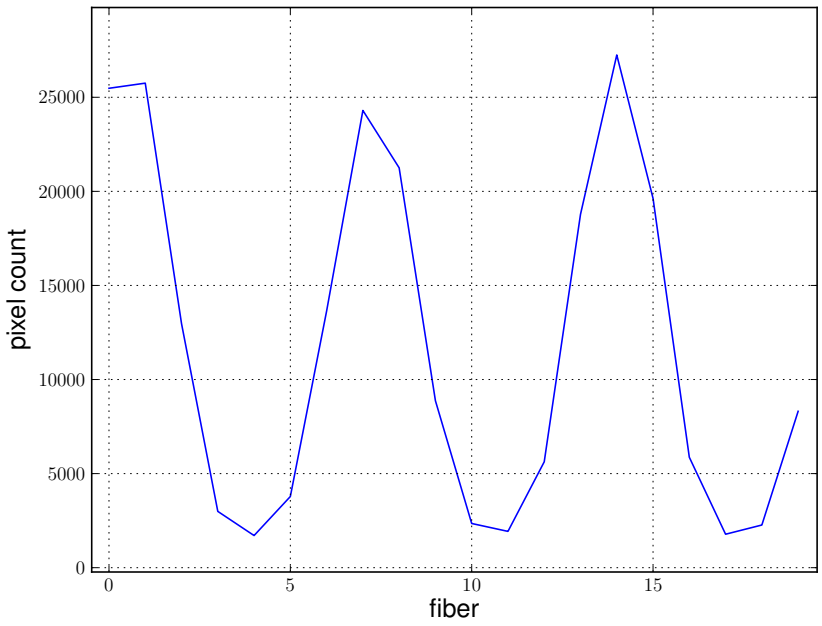

Figure 2.4: Cross-sectional profile across one bundle of a CCD

continuous rows. As a result the PSF in different rows will overlap with each other. Both Boxcar and Optimal extraction do not correct for blending.

2.4 Inverse Variance

Read-out noise in a pixel is introduced in the system due to amplifier noise [24]. The counts (N) in a pixel are composed of actual electrons proportional to the pixel intensity at that pixel and the counts generated in that pixel by shot noise. Shot noise is random fluctuation in the number of photons arriving.

The variance for flux in every pixel k is given by

$$V_k = \langle N_k \rangle + r_k^2 \tag{2.10}$$

where, N_k is the number of counts in pixel k

r_k is the readout noise.

Shot noise has Poisson distribution and in the case of large N, the Poisson approaches the Gaussian distribution. The standard deviation or the uncertainty (error) associated with any pixel is given by,

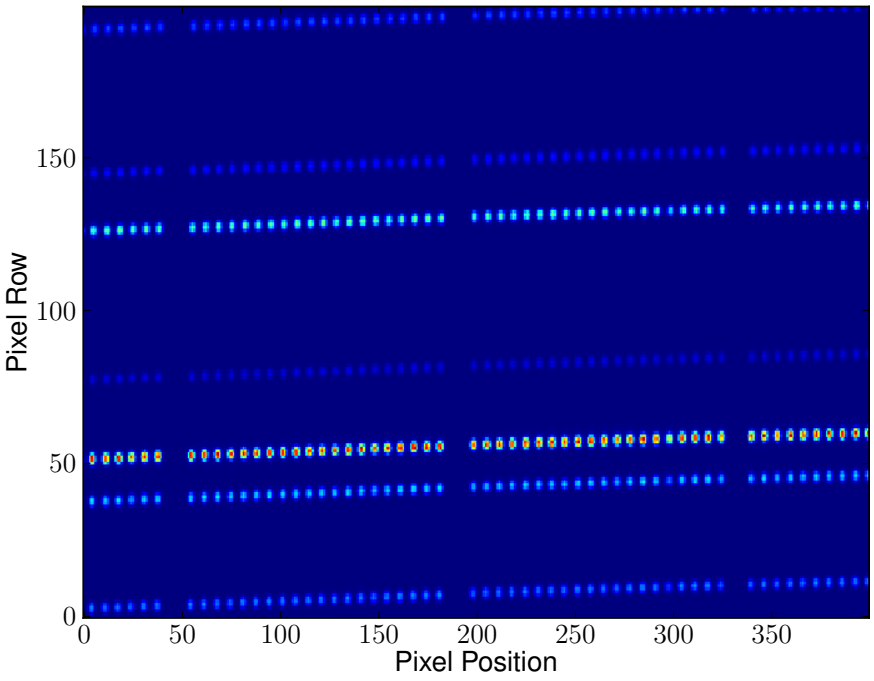

Figure 2.5: Arc image

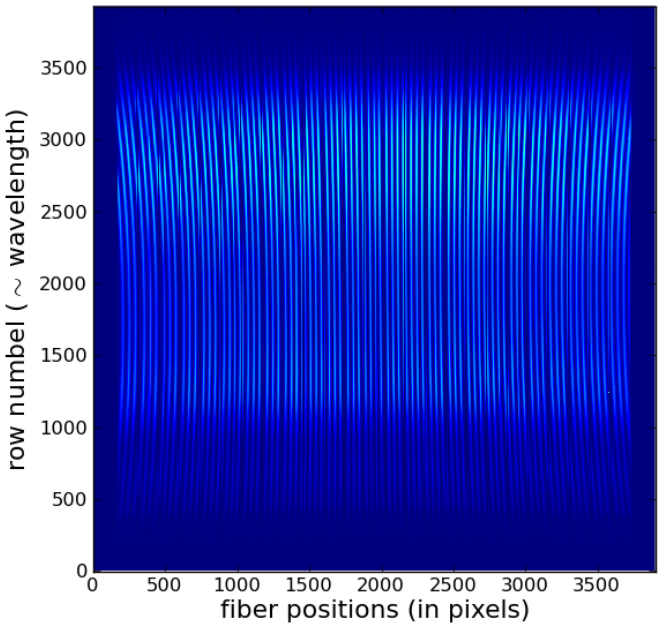

Figure 2.6: Flat-field image

$$E_k = \sqrt{V_k} \tag{2.11}$$

Inverse Noise (IN) of any pixel k is defined as,

$$IN_k = \frac{1}{E_k} \tag{2.12}$$

Inverse Variance (IVR) of any pixel k is defined as,

$$IVR_k = IN_k^2 \tag{2.13}$$

or it can be written as,

$$IVR_k = V_k \tag{2.14}$$

Any pixel with high error value will have low inverse noise and as a result it has low inverse variance and vice versa. Hence, inverse variance is used to weight pixels. Any pixel with higher value of error than others is given lower weight.

2.4.1 System Calibration Matrix

We assume our CCD detector to be a linear device because as the intensity of the light recorded by a pixel increases the counts generated in that pixel increase. For the case of a linear CCD we can model the counts at a particular pixel l from fiber k at a wavelength w as,

$$p_l = \sum_h A_{l,h} f_h + n_l, \tag{2.15}$$

where, h indexes all combinations of (k,w) pairs.

Here, f_h represents the flux in fiber k at wavelength w and n_l represent additive noise in pixel l. Note that we have suppressed the two-dimensionality of the CCD by allowing l to index all pixel positions (i,j). Also, we use h to index all (k, w) pairs.

The model given by (2.15) can be conveniently written in matrix form as,

$$\mathbf{p} = \mathbf{A}\mathbf{f} + \mathbf{n}, \tag{2.16}$$

Our aim is to estimate flux $\mathbf{f}$ of an astronomical object, which requires the knowledge of $\mathbf{A}$. To estimate $\mathbf{A}$ we model the 2D PSF as a function of fiber and wavelength. We use arc-images for modeling the PSFs as they are well separated

from each other and there is no cross-talk from neighboring PSFs. Once we have estimated $\mathbf{A}$, we can use its knowledge to estimate $\mathbf{f}$ in science data which includes on-sky galaxies, quasars, stars, etc. We have seen in Fig.1.4 ("Arc") that the PSFs at different wavelengths are well defined and do not overlap with each other. Hence, these images are used to model the PSFs as function of fiber number and wavelength.

CHAPTER 3

2D PSF CALIBRATION

We present a technique that aims to overcome the shortcomings of the optimal extraction method. As discussed earlier when light from an optical fiber at a particular wavelength falls on the CCD it forms a 2D image called the point spread function. In this technique we model the 2D image as a whole, contrary to the optimal extraction method which models it row-by-row [5]. This technique also takes into account the superposition of different PSFs from the same fiber but at different wavelengths. In further sections we will also see that our model is valid for all classes of PSFs contrary to row-wise extraction which is valid only for separable PSFs.

3.1 Modeling Approach

We estimate the system calibration matrix separately for different wavelength. In addition, we estimate the system calibration matrix separately for different bundles. In other words, we model the PSFs together formed at a particular wavelength from fibers belonging to a particular bundle. This is based on the assumption that the profile of the PSFs at a wavelength is approximately similar within the bundle. From (2.15) since, w is fixed h indexes only k. Consequently, $\mathbf{A}$, the calibration matrix, at a particular wavelength would consist of elements, $[A_{l,k}]$ where $k = 1 \ldots, 20$ represents the fiber at the considered wavelength. Similarly, we estimate the value of $\mathbf{A}$ separately for different wavelengths and a different fiber bundle.

For the purpose of the estimation of calibration matrix $\mathbf{A}$ we use arc-images. Arc-images have a special property where the PSFs are well separated for different wavelengths. This enables us to estimate the calibration matrix separately for different wavelengths. Moreover, all the fibers in the arc-images carry the same flux for a particular wavelength. Thus, we can actually estimate the system calibration matrix

for a *unit* of flux. The next section explains the estimation of system calibration matrix the PSF is assumed to have a Gaussian profile.

3.1.1 Implementation of 2D Gaussian Calibration Analysis on Arc-data

This section explains the estimation of calibration matrix **A** at a particular wavelength in a bundle. Each bundle has 20 fibers, so light from each fiber at a wavelength will form a PSF. So we model 20 PSFs at a particular wavelength together. We assume that the contribution of PSF for a fiber k would extend to a relatively small region around the centroid of the PSF of fiber k. In our implementation we assume it extends to 10 pixels on either side of the x and y direction from the centroid of the PSF. We propose to model the PSF from a fiber k as a 2D Gaussian function, given as,

$$B_{l,k} = \frac{1}{2\pi\sigma^2} e^{-\frac{1}{2}\left[\frac{(x_l - x_c^k)^2 + (y_l - y_c^k)^2}{\sigma^2}\right]} \tag{3.1}$$

where,

- nonzero values of x_l varies from $(x_c^k - 10) < x_l < (x_c^k - 10)$
- nonzero values of y_l varies from $(y_c^k - 10) < y_l < (y_c^k - 10)$
- x_c^k: x-centroid for fiber k,
- y_c^k: y-centroid for fiber k,
- σ : width of the Gaussian core which is same for all fibers of a bundle at a particular wavelength

Different optical fibers have different throughput. Even though the arc-lamps which are used to construct calibration images have the same flux, the flux of light which falls on the CCD pixels varies from one fiber to another due to difference in fiber throughput. As a result the pixel count values which are produced when the light hits the CCD also vary with fiber.

Consequently we scale each PSF at a particular fiber k with r^k which represents the relative fiber-fiber throughput contribution.

$$\langle r_k \rangle = 1 \tag{3.2}$$

where, $\langle\rangle$ represents ensemble mean. Let A_l^k defines the noise free count value at pixel l when light of *unit* flux falls on it from fiber k.

$$A_{l,k} = r^k B_l^k, \tag{3.3}$$

As given in (2.16), the observed CCD pixel count at pixel l is given as,

$$p_l = \sum_k A_{l,k} f_k + n_l, \tag{3.4}$$

By substituting the value of $A_{l,k}$ from (3.3) we get,

$$p_l = \sum_k \left(r^k B_l^k \right) f_k + n_l, \tag{3.5}$$

The system calibration matrix for 2D Gaussian is given by (3.3). However, we need to evaluate its performance and also see if it perfectly models the PSF. For this we evaluate its performance on arc-images. The model count value at pixel l for an arc-image is then given as:

$$M_l = \sum_k A_{l,k} f_k, \tag{3.6}$$

where, f_k is the input spectrum of fiber k.

The minimum χ^2 solution for $\mathbf{f}$ from the data vector $\mathbf{p}$ is given by [25] [26]

$$\mathbf{f} = (\mathbf{A^T N^{-1} A})^{-1} \mathbf{A^T N^{-1} p}, \tag{3.7}$$

where, $\mathbf{N}$ is a pixel noise matrix. We treat raw pixel errors as statistically independent and, thus, the noise matrix is diagonal matrix. Value of $\mathbf{f}$ gives us the estimate of flux in different fibers at a particular wavelength. In the next section we evaluate the 2D Gaussian PSF on an example image and analyse the efficiency of the PSF model in capturing the features of 2D PSF.

3.1.2 Results of Using 2D Gaussian Profile to Model PSF

In this section we evaluate the performance of 2D Gaussian model on an example image shown in Fig. 3.1. This image shows PSFs at a wavelength in a bundle. This image region is chosen such that it includes all 20 PSFs. This image region is of size 41 $\times$ 150 pixels. In Fig. 3.2 we show the model image constructed using a circular 2D Gaussian profile with the estimated parameters. In Fig. 3.3 we show the residuals of subtraction of the 2D Gaussian model and data. These residuals show

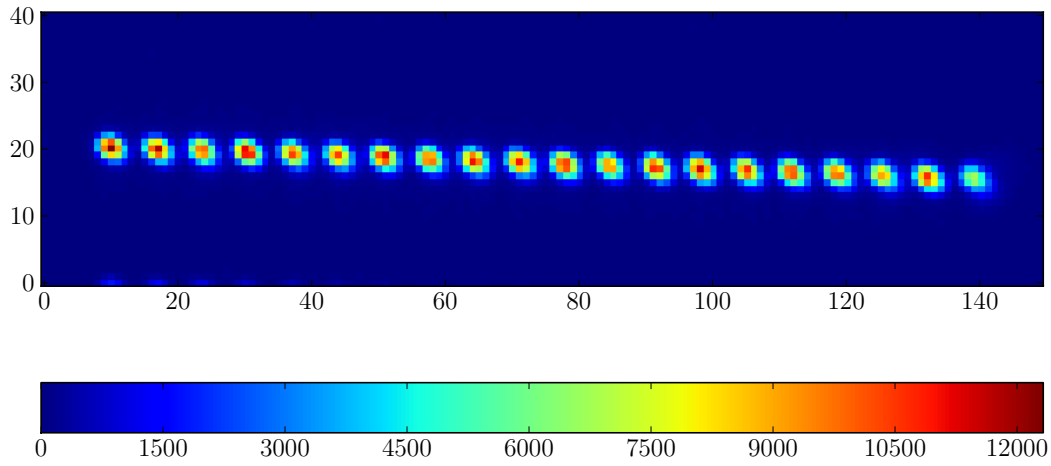

Figure 3.1: Example data region for estimation of calibration matrix at a particular wavelength

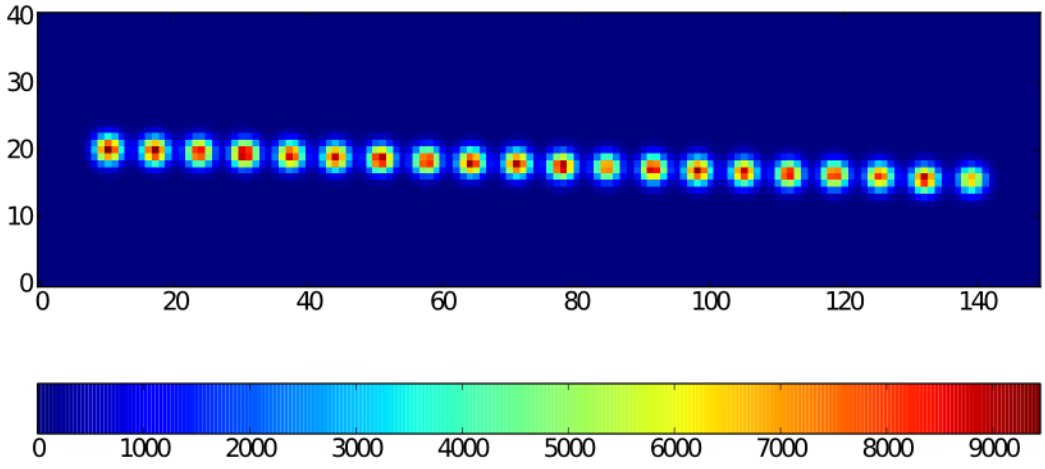

Figure 3.2: Model constructed using 2D Gaussian profile for the PSF

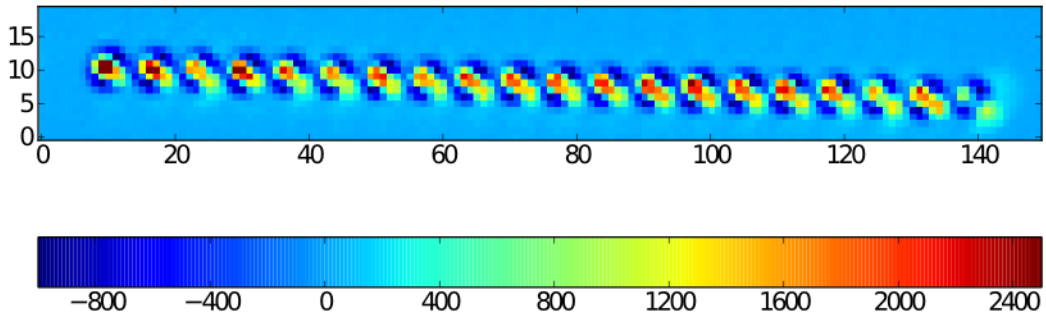

Figure 3.3: Residuals for 2D Gaussian Model

that the model is not able to capture the skewness and the ellipticity in the PSF. The pattern in the residual values indicates high positive values (indicated by red color) along the diagonal in the upper left quadrant and it decays as it move towards the southwestern direction. Since the residual is obtained by subtraction of model from data and our model is radially symmetric we attribute this pattern in residual to asymmetric distribution of values in data. The asymmetric values indicate skewness in data PSFs. The model being symmetric is not able to capture this skewness.

In each PSF we see two regions, an under-subtracted (positive region) and an over-subtracted region (negative values). The under-subtracted region indicates that at these places the value of model is low as compared to the data. Moreover, the data have higher values at an angle from the center of the PSF. The symmetrical Gaussian has higher values along the vertical diagonals. Due to this 'tilt' in data we observe the under-subtracted region at an angle of 45 from the center of the PSF. A closer look at the PSF of this image in Fig.3.4(b) shows the tilt in the PSF.

Figure 3.5(a) shows another image section at the center of the CCD. Fig. 3.5(b) shows a PSF of this image section. In this PSF we do not see the amount of ellipticity and skewness as in 3.4(b). In fact, as we move from the center of the CCD to its edges, the skewness of the PSF increases. This is because of various optical aberrations like spherical aberration, astigmatism and coma [4] in the CCD instrument. Hence, we

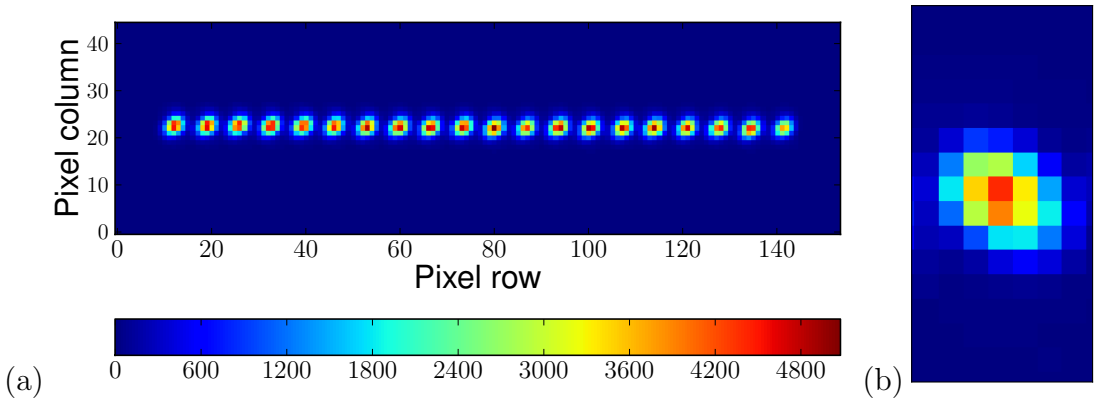

Figure 3.4: A data region at the edge of the CCD and by zooming on one of the PSFs

need an efficient model which is able to capture both the ellipticity and skewness in the data. In the next section, we present one such model.

3.2 Gauss-Hermite Formulaism for PSF Decomposition

In this section we explain the modeling of the 2D the point spread functions PSF using a Gauss-Hermite polynomial [27, 28]. The Gauss-Hermite function is formed when Hermite polynomials are multiplied with 2D Gaussian function to change

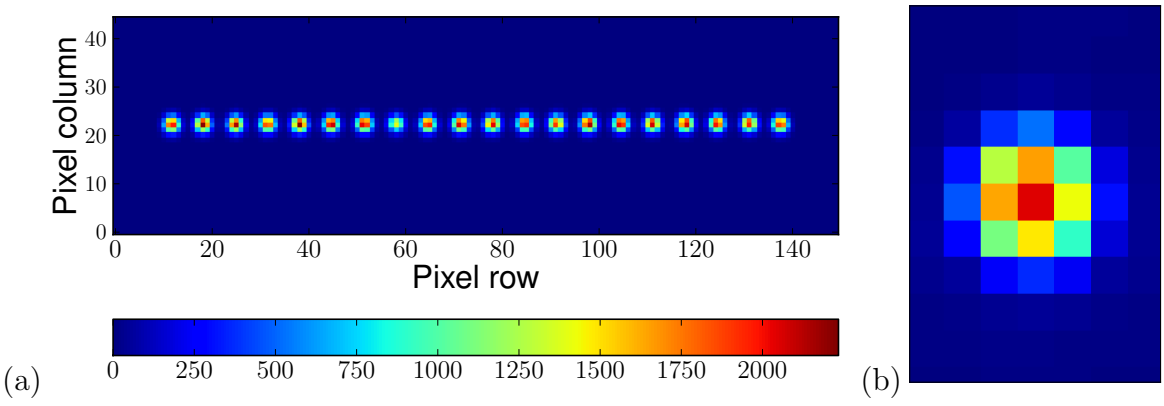

Figure 3.5: A data region at the center of the CCD and by zooming on one of the PSFs

its shape in the x and y direction, but at the same time maintaining its Gaussian structure. The Gauss-Hermite polynomial of order (m, n) is represented as

$$g(m,n) = \frac{1}{2\pi\sigma^2} H_m(\frac{x}{\sigma}) H_n(\frac{y}{\sigma}) e^{-\frac{1}{2}\left[\frac{x^2+y^2}{\sigma^2}\right]} \tag{3.8}$$

where,

- $H_m(x)$: Hermite polynomial of order 'm' in the x direction
- $H_n(y)$: Hermite polynomial of order 'n' in the y direction
- $e^{-\frac{1}{2}\left[\frac{x^2+y^2}{\sigma^2}\right]}$: 2D Gaussian core

The Hermite polynomial (probabilists' Hermite polynomial) of order n is given by:

$$H_n(x) = (-1)^n e^{x^2/2} \frac{d^n}{dx^n} e^{-x^2/2} \tag{3.9}$$

3.2.1 Orders of Hermite Polynomial

The Gauss-Hermite function for order (0,0), $g(0,0)$ is essentially a 2D Gaussian core. Different orders when multiplied with the 2D Gaussian core determine its profile in the x and y direction.

The properties of different orders of Gauss-Hermite function can be summarized as:

1. Order 1 provide corrections to the Gaussian centroid.
2. Order 2 provide corrections to the Gaussian sigma.
3. Order 3 provide corrections to the skewness of the Gaussian core.
4. Order 4 provide corrections to the kurtosis of the Gaussian core.

Order 2 of Gauss-Hermite polynomials either increases or decreases the Gaussian sigma value. Fig. 3.6(a) shows the symmetrical Gaussian core that is Gauss-Hermite order (0,0). Now when weighted Gauss-Hermite of order (2,0) is added to the Gaussian core Fig. 3.6(a), the resultant profile as represented in Fig. 3.6(b) is wider in the x-direction. Similarly when a Gauss-Hermite polynomial of order (0,2) is added to order (0,0) the width increases in y-direction as given by Fig. 3.6(c).

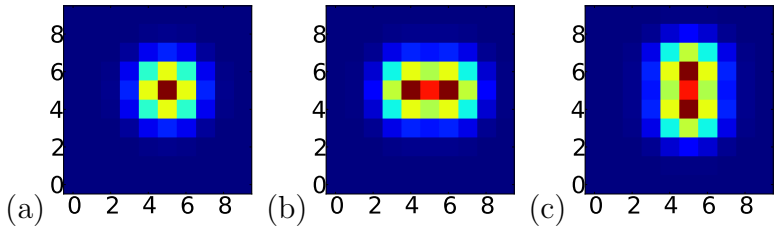

Figure 3.6: Profile of order (0,0), symmetrical Gaussian profile (b)Profile of order (2,0) added to order (0,0) (c)Profile of order (0,2) added to order (0,0)

Order (1,1) adds ellipticity with a tilt at 45° to the x-direction. Fig. 3.7(b) shows the resultant profile when a weighted Gauss-Hermite order (1,1) is added to order (0,0) in Fig. 3.7(a). When the weight to order (1,1) is negative the ellipticity is at 135°.

In Fig. 3.8 we see the profile obtained on adding order (0,0) to weighted order (0,3). Order (0,3) adds skewness to the symmetrical Gaussian profile. We can see that the PSF decays faster on the left of pixel (5,5). It is heavy-tailed on the right of pixel (5,5) in the spatial domain. Due to the skewness, the PSF is no longer radially symmetric.

3.2.2 Implementation of Gauss-Hermite Calibration Analysis on Arc-data

This section explains the modeling of the 2D PSF using the Gauss-Hermite function. We model the PSF from a fiber k at a particular wavelength as a weighted linear combination of different orders of the Gauss-Hermite functions. Our model of

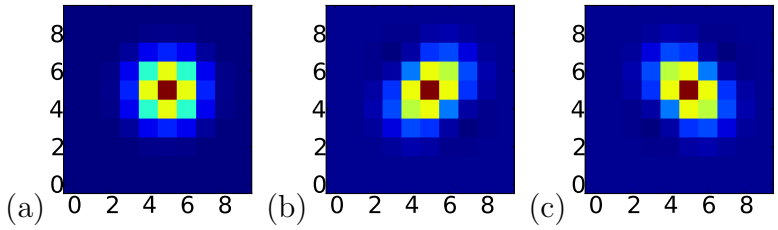

.

Figure 3.7: Profile of order (0,0), symmetrical Gaussian profile (b)Profile of order (1,1) is added to order (0,0) (c)Profile of order (1,1) is subtracted from order (0,0)

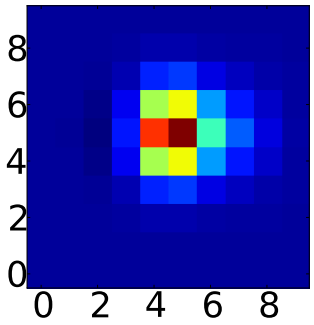

Figure 3.8: Resultant PSF when a Gauss-Hermite order (0,3) is added to 2D symmetric Gaussian given by order (0,0)

a 2D PSF from fiber k at a particular wavelength is given as

$$v_l^k(m,n) = \frac{1}{2\pi\sigma^2} H_m(\frac{x_l - x_c^k}{\sigma}) H_n(\frac{y_l - y_c^k}{\sigma}) e^{-\frac{1}{2}\left[\frac{(x_l - x_c^k)^2 + (y_l - y_c^k)^2}{\sigma^2}\right]} \tag{3.10}$$

where,

- nonzero values of x_l varies from $(x_c^k - 10) < x_l < (x_c^k - 10)$
- nonzero values of y_l varies from $(y_c^k - 10) < y_l < (y_c^k - 10)$
- $H_m(x)$: Hermite polynomial of order 'm' in the x direction
- $H_n(y)$: Hermite polynomial of order 'n' in the y direction
- σ: width of the Gaussian core, it is same for all fibers at a wavelength
- x_c^k: x-centroid for fiber k
- y_c^k: y-centroid for fiber k

Note that the orders are taken such that $m + n \leqslant 4$. In other words, there are 15 different combinations of the order pair (m, n). These Gauss-Hermite orders modify the shape of PSF in x and y direction.

Let t be a variable that indexes all orders (m, n) of the Gauss-Hermite function and c_t represents the weight to the Gauss-Hermite function of order index t. The Gauss-Hermite weight of order (0,0) (c_0) gives the flux in a fiber at a wavelength.

Since the system calibration matrix is constructed for a unit flux, the value of c_0 is one. The other weights to Gauss-Hermite determine the shape of PSF. Let r^k represent the relative fiber-fiber throughput contribution.

The noise free count value at pixel l from fiber k is given as:

$$A_{l,k} = r^k \sum_t c_t v_l^k(t) \tag{3.11}$$

where, $A_{l,k}$ is the $(l,k)^{th}$ element of the system calibration matrix.

By substituting the value of $A_{l,k}$ from (3.11) in (2.16), observed CCD pixel count at pixel l is modeled as,

$$p_l = \sum_k r^k \left(\sum_t c_t v_l^k(t) \right) f_k + n_l \tag{3.12}$$

3.2.3 Estimation of Weights for Gauss-Hermite Orders

This section explains the estimation of the weights for different Gauss-Hermite orders. Combining (3.6) and (3.12) we get,

$$M_l = \sum_k r^k \left(\sum_t c_t v_l^k(t) \right) f_k \tag{3.13}$$

Since for arc-images the input flux is constant for all fibers, , $f_k = f$ for all k's, the model can be written as,

$$M_l = f \sum_k r^k \left(\sum_t c_t v_l^k(t) \right) \tag{3.14}$$

By changing the order of summation we get

$$M_l = f \sum_t \left(\sum_k r^k v_l^k(t) \right) c_t \tag{3.15}$$

The inner summation sums the contribution of all fibers for a particular order, which is denoted by $\Theta_{l,t}$

$$\Theta_{l,t} = \sum_k r_k v_l^k(t) \tag{3.16}$$

The model can be represented as

$$M_l = f \sum_t \Theta_{l,t} c_t \tag{3.17}$$

$$M_l = \sum_t \Theta_{l,t} \tilde{c}_t \tag{3.18}$$

where, $\tilde{c}_t = f c_t$

In vector notation it can be represented as,

$$\mathbf{M} = \mathbf{\Theta}\check{\mathbf{c}} \tag{3.19}$$

Now, the minimum χ^2 solution for vector $\tilde{\mathbf{c}}$, from the data vector $\mathbf{p}$ is given by

$$\hat{\mathbf{c}} = (\mathbf{\Theta^T N^{-1} \Theta})^{-1} \mathbf{\Theta^T N^{-1} p}, \tag{3.20}$$

where, $\hat{\mathbf{c}}$ is the estimated value of $\tilde{\mathbf{c}}$. Here, $\mathbf{N}$ is a pixel noise matrix.

The system calibration matrix is defined when light of unit flux falls on the CCD. The arc-lamp used to construct the arc-calibration images have a constant flux, greater than unity. The estimated value of flux in arc-lamps at a particular wavelength is given by the amplitude of PSF. Coefficient $\hat{c}_0$ ($t = 0$, $(m, n) = (0,0)$) gives the value of the amplitude or flux of the PSF and the remaining coefficients determine the shape of PSF. To estimate the value of weights to Gauss-Hermite orders ($\mathbf{c}$) when light of unit flux falls on the CCD, we divide $\hat{\mathbf{c}}$ with $\hat{c}_0$. The resulting value is the estimated value of $\mathbf{c}$ which is used to construct the system calibration matrix.

3.2.4 Estimating the Weights to Gauss-Hermite Orders at all Wavelengths

In the previous section we estimated weight to Gauss-Hermite orders at a few distinct wavelengths as the arc-images form PSFs only at a few distinct wavelengths. Our next goal is to estimate weights to Gauss-Hermite orders at all wavelengths. We expect the value of weights to be a smooth function of wavelength.

Fig. 3.9 shows the variation of weight to Gauss-Hermite polynomial of order (1,1) with wavelength. The wavelength axis consists of all the known wavelengths in the arc lamp spectrum. We observe the value of weights varying as a smooth function of wavelengths although there are few outliers. At these outliers the value of weights either increases/decreases abruptly. This abrupt behavior in the weights is observed for all the orders of the Gauss-Hermite polynomial and at the same wavelengths. This abrupt behavior in the weights occurs primarily for two reasons:

1. the pixel count value at these wavelength is very low.

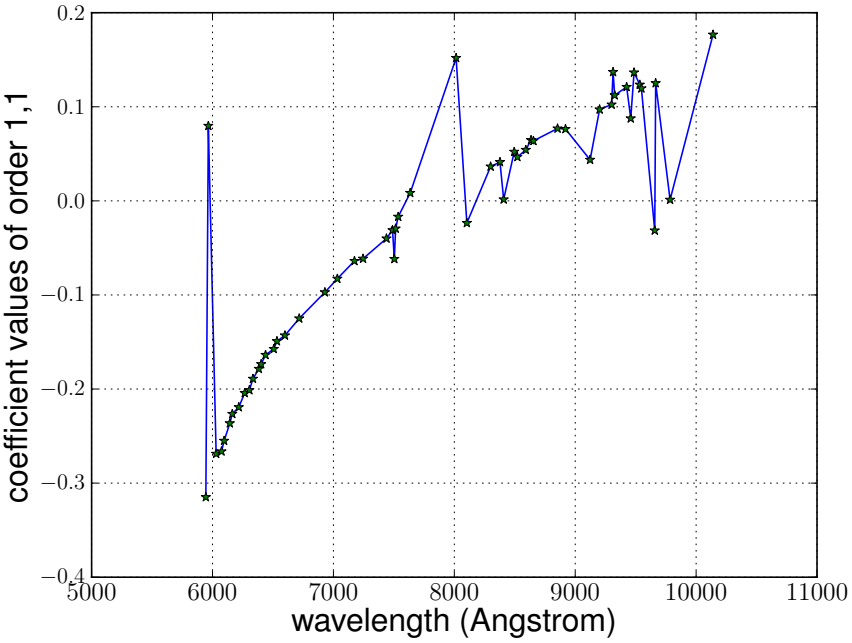

Figure 3.9: Variation of value of coefficient of order: (1,1) with the known wavelengths

2. the PSFs at these wavelengths are *blended* with PSFs at the adjacent wavelengths.

The pixel count value is directly proportional to the number of photons hitting the CCD. So if the number of photons hitting the pixel is low the pixel count value is also low. We observe low count at specific wavelengths and this phenomenon is seen across the exact same wavelengths in all the images that we have tested. This phenomenon is due to shortcomings in the arc-lamps which causes them to emit low photon counts at few wavelengths. Also, few wavelengths at which arc-lamp emit light are very close to each other. As a result the effect of the PSFs from these wavelengths are also present in the nearby rows on the CCD. This causes the PSFs to overlap with each other and we call this phenomenon *blending*.

The weight to the Gauss-Hermite coefficients for wavelength 8000 $\mathring{A}$ in Fig. 3.9 has very high value. The PSFs modeled at this wavelength are the PSF row, centered at row number 20 in the image. Fig. 3.10 shows the image region at this wavelength. The color scale of the image has been adjusted from 0 to 90 to show the low count values across row 20. The typical peak pixel count value of arc-images is around

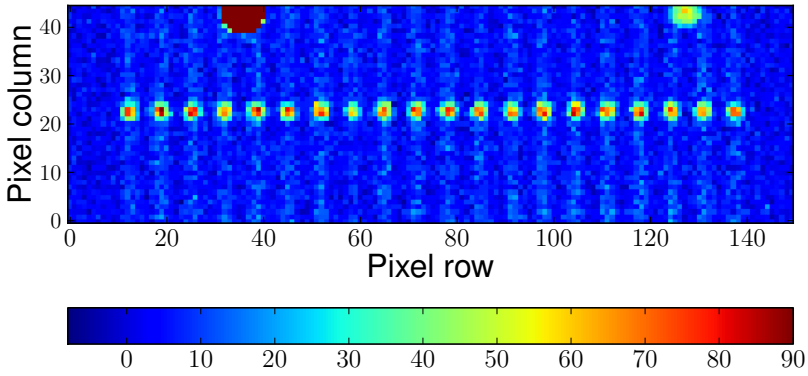

Figure 3.10: Example image region where the data count is very low

1000 whereas the pixel count values of the PSFs at row 20 are very low, less than 90. Hence, the data in these regions are not sufficient for the coefficient value to be determined accurately.

An example of an image region at $\lambda = 8014$ $\mathring{A}$ is shown in Fig. 3.11. The PSFs modeled at this wavelength is the PSF row, centered at row number 20. The PSFs in this row blend with the PSF at the wavelength(row) below it. The blending indicates that the PSF in adjacent rows overlap with each other and the model tries to fit both the PSF rows together. As a result of this we get very high value of coefficients which is a deviation from the expected behavior.

The arc-lamps emit light only at few distinct wavelengths. Once we have determined the values of coefficients at specific wavelengths using calibration frames, we

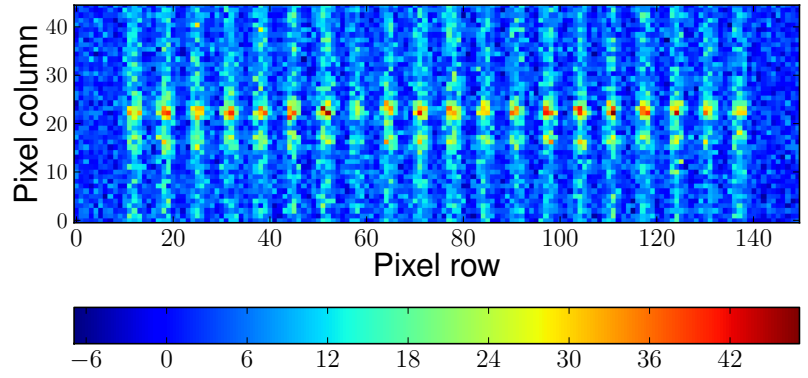

Figure 3.11: Example image region showing blending of PSFs

have to estimate values at the entire wavelength range of the CCD. This can be done by fitting a polynomial to the known coefficients values [29]. For this we mask the value of weights which are outliers and fit a polynomial of degree three to the known values. Figure 3.12 indicates polynomial fit to coefficient values of a bundle at all the known wavelengths.

3.2.5 Modified Gauss-Hermite PSF Model

In the previous section we presented a model for modeling the PSF as a linear combination of different orders of the Gauss-Hermite function, such that the sum of orders is less than or equal to four. We initially assume a 2D Gaussian profile for the PSF and try to optimize its parameters, width (σ^k) and centroid (x_c^k, y_c^k) by using a nonlinear optimization technique. The estimated values of these parameters in the Gauss-Hermite model are assumed as their initial values in the modified Gauss-Hermite model. The order (0,1) and (1,0) of Gauss-Hermite polynomial give corrections to x and y centroids and (0,2) and (2,0) provide the corrections to Gaussian width. Since these parameters have already been optimized we can exclude

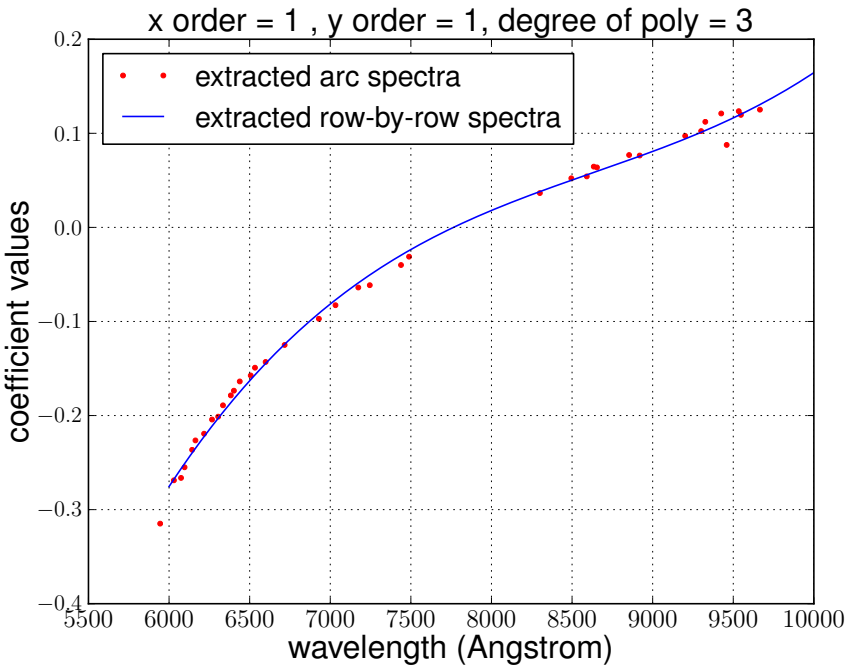

Figure 3.12: Polynomial fitting to coefficients of Order (1,1)

Gauss-Hermite orders (0,1), (1,0), (0,2) and (2,0) although we include difference of orders (2,0) and (0,2) in our model.

As a result, the number of parameters to be estimated decreases from 15 to 12 in this case.

The basis function is given by

$$\mathbf{A} = [B_{0,0}, B_{diff}, B_{0,3}, B_{0,4}, \ldots B_{4,0}] \tag{3.21}$$

where,

$$B_{diff} = (B_{0,2} - B_{2,0})] \tag{3.22}$$

As seen in Section 3.2.1 Fig. 3.7 order (1,1) provides ellipticity with a tilt of 45° to the PSF. In addition, order B_{diff} ((2,0 - 0,2)) is roughly equal to the order (1,1) rotated by 45°. Order B_{diff} increase the ellipticity of the PSF in x or y directions. A combination of order (1,1) and order B_{diff} gives us ellipticity with arbitrary angle of tilt. We need this behaviour as different PSF across the CCD image have different 'tilt' and a combination of order (1,1) and B_{diff} will help us in getting this behaviour. Figure 3.14(a) shows the PSF obtained after adding weighted order (1,1) to circular Gaussian PSF. These figures have been represented in nonpixelized forms to shows the tilt in the PSFs clearly. We see the tilt is at an angle 45° from the x-axis of the PSF. Figure 3.13 show the order (1,1) and order B_{diff}. Figure 3.14(b) shows the PSF

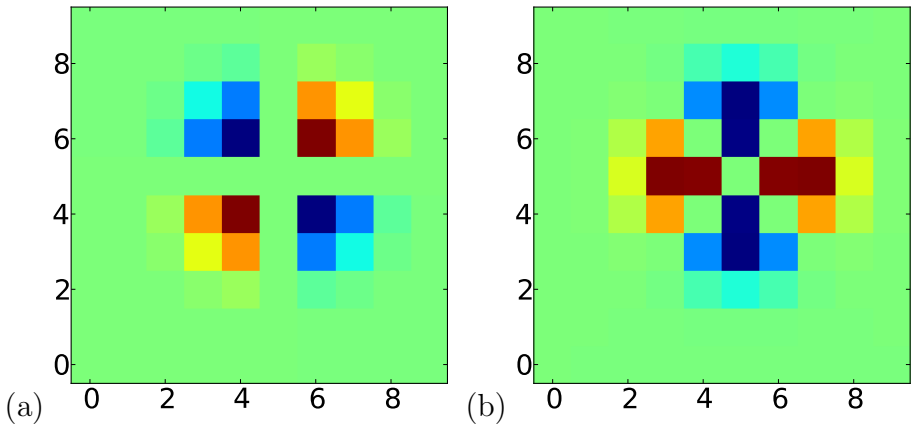

Figure 3.13: Order (1,1) and Order (2,0 - 0,2)

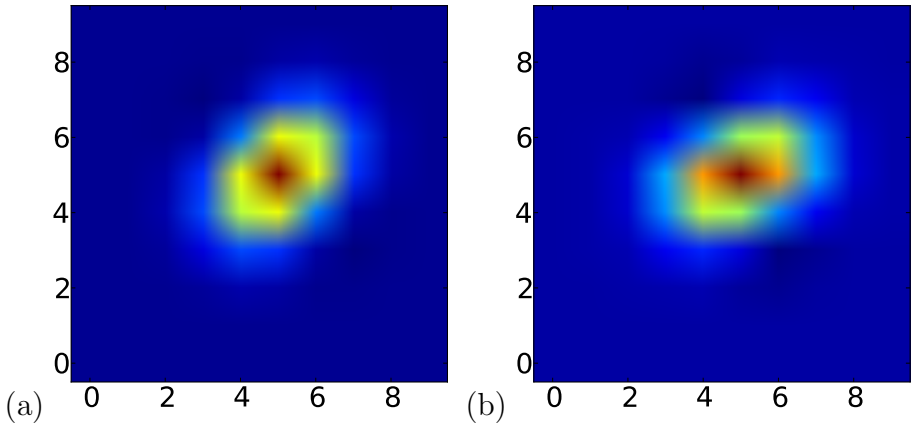

Figure 3.14: Ellipticity with tilt at 45° and ellipticity with tilt less than 45°

when both B_{diff} and order (1,1) are added to circular Gaussian profile. We can see that the tilt is now at an angle less than 45°.

3.3 Quantitative Comparison of Various Models for 2D PSF

The comparison of the quality of Gauss-Hermite Modified Gauss-Hermite model PSF models is done by calculating the average χ^2 value for the whole image. The χ^2 value is defined as the

$$\chi^2 = \sum_i \left[\frac{(p_i - M_i)^2}{n_i^2} \right] \tag{3.23}$$

Here, the p_i are the raw pixel data values, M_i are the model values in those pixels, n_i are the noise values in those pixels. We define average χ^2 as the mean value of χ^2 over all the wavelengths and bundles in the calibration image.

Fig. 3.15 shows the model constructed by using a Gauss-Hermite profile for the PSF. We can see that this model shows higher values of skewness and ellipticity in comparison to the model of Fig. 3.2.

Fig. 3.16 shows the residuals by subtracting the Gauss-Hermite model from the data. In the residuals for Gauss-hermite models we do not observe any high positive value region in any of the quadrant of the PSF as seen in Fig. 3.3 (indicated by red color) and the values in Fig. 3.16 are mostly uniformly distributed. This indicates that the Gauss-Hermite model is able to capture the skewness in model. Also, there

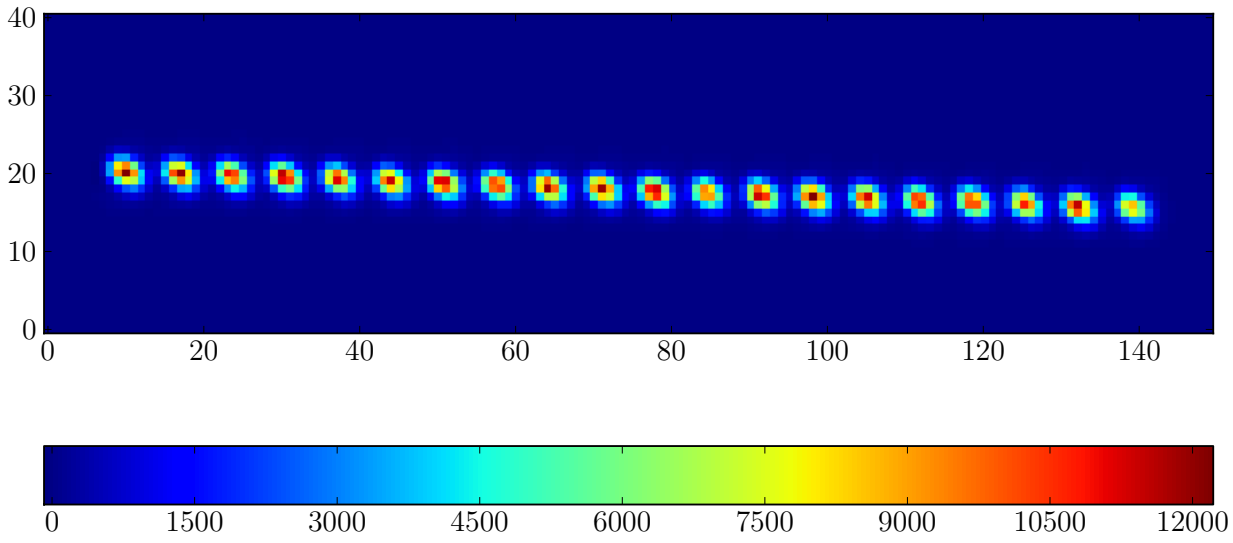

Figure 3.15: Gauss-Hermite model

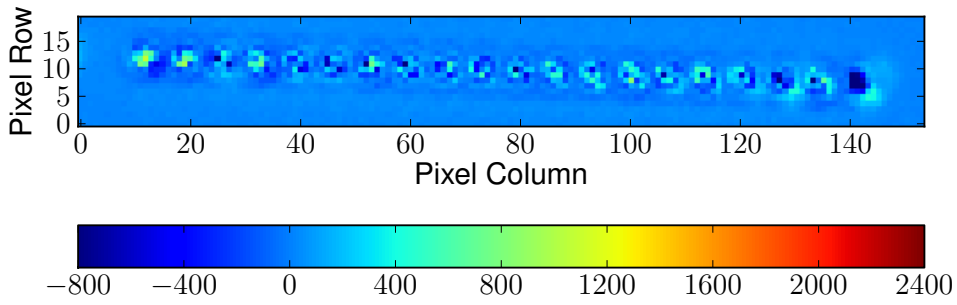

Figure 3.16: Residuals for Gauss-Hermite model

are no two distinct regions, under-subtracted and over-subtracted regions, as in the case of Fig. 3.3. This indicates that the model is able to capture the ellipticity in data. Hence, the Gauss-Hermite model capture the data better than the circular 2D Gaussian model.

Table 3.1 shows the comparison of reduced χ^2 for various PSF models. Although the performance of modified Gauss-Hermite model decreases by 12.21% in comparison to Gauss-Hermite model, its complexity decreases by 20% due to reduction in number of parameters from 15 to 12. This is because the the modified Gauss-Hermite model does not optimize the value of orders (0,1),(1,0),(2,0),(0,2) and assumes them to fixed parameters. These values of fixed parameters, width and centroid are obtained by

Table 3.1: Table Showing Comparison of Reduced χ^2 for Various PSF Models

Model	Circular Gaussian	Gauss-Hermite	Mod. Gauss-Her
Reduced χ^2: example image region	165.32	25.27	41.403
Reduced χ^2: whole image	25.88	15.48	17.37

optimizing them by assuming a 2D Gaussian profile for the PSF. This assumption is not true as the PSF is not necessarily a Gaussian over the entire CCD image.

The region where the PSF core is elliptical (in the example image) the improvement is 84.71% in comparison to the 2D Gaussian model. This shows that the model performs very well in comparison to the 2D Gaussian model in the image regions where the PSF is tilted. The improvement for the entire image in χ^2 when Gauss-Hermite model is used is around 40%.

3.4 Modeling of Wing Component

Fig. 3.17 is obtained by adjusting the color scale of Fig. 3.16. We observe under-subtracted (positive and yellow in color) regions around *each* PSF core. We call these 'halo' regions surrounding the core of the PSF wings. Fig. 3.17 shows the halo and the core regions. These regions indicate that the Gauss-Hermite model is unable to model the wings accurately. In these halo regions the data values are greater than the model. Hence, we need a slowly decaying spatial profile to model these wings component. Our next step is to incorporate a wing model while modeling the core of 2D PSF.

3.4.1 One-Dimensional Wing Profile

Figure 3.18 shows the one dimensional flux profile. The counts are plotted in log_{10} scale. We can clearly see the core and the 'wing' component in this profile. For estimation of parameters, flux and width of the wing profile we use a kind of frames called as sparse frames. These frames have only one fiber plugged per bundle and hence the plugged in fiber does not experience any cross-talk from neighboring fibers. Figure 3.19 shows sparse flats and Fig. 3.20 shows the arc flats. We use sparse flats in our analysis because they have higher signal to noise ratio in comparison to sparse

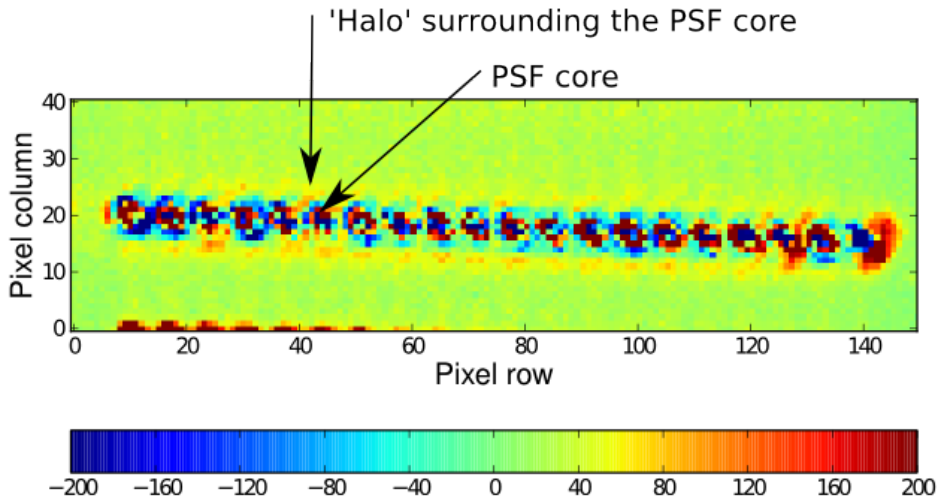

Figure 3.17: Residuals from Gauss-Hermite Model

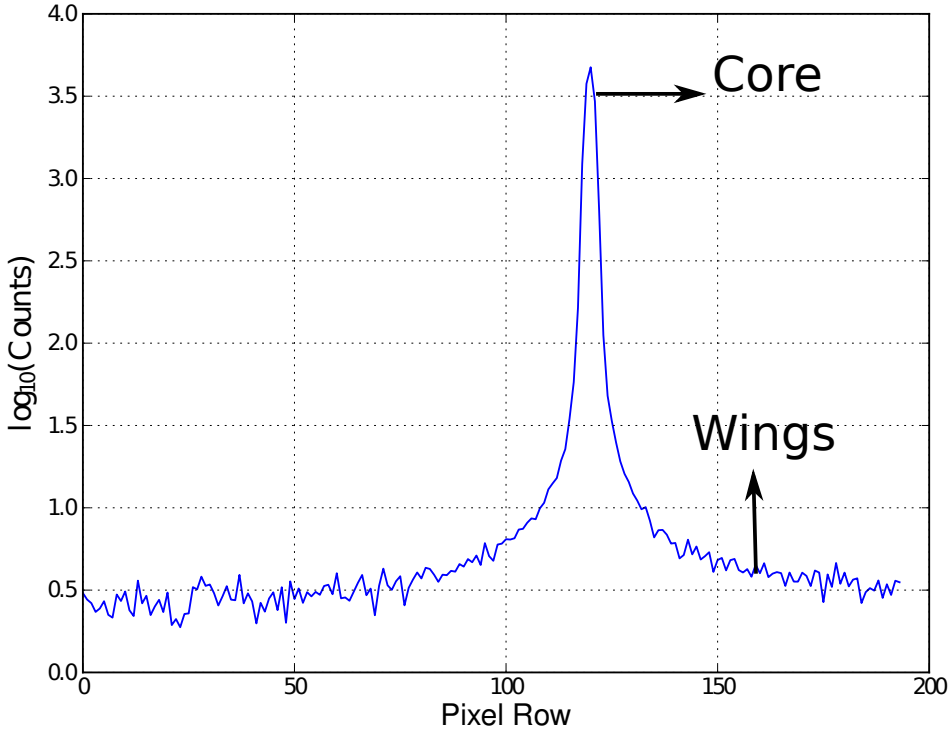

Figure 3.18: One-Dimensional flux profile of a fiber at a particular wavelength

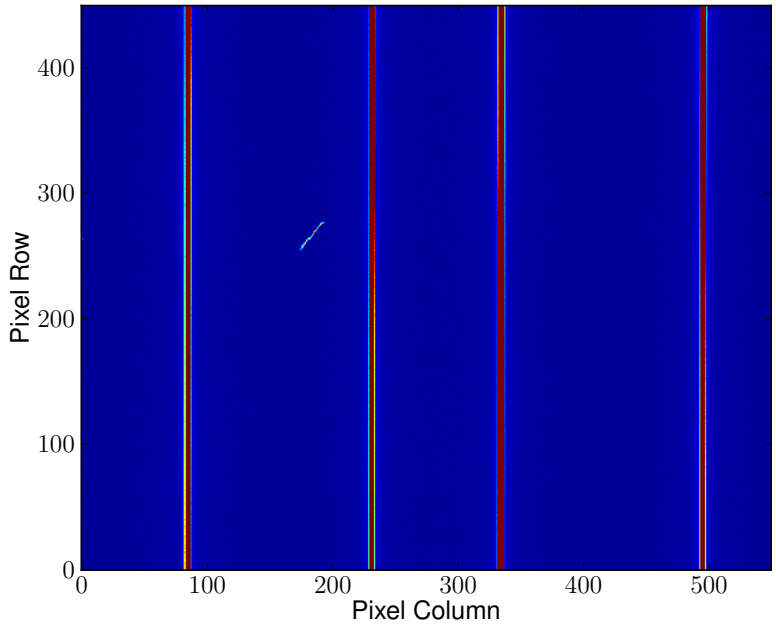

Figure 3.19: Sparsely plugged flat-field image

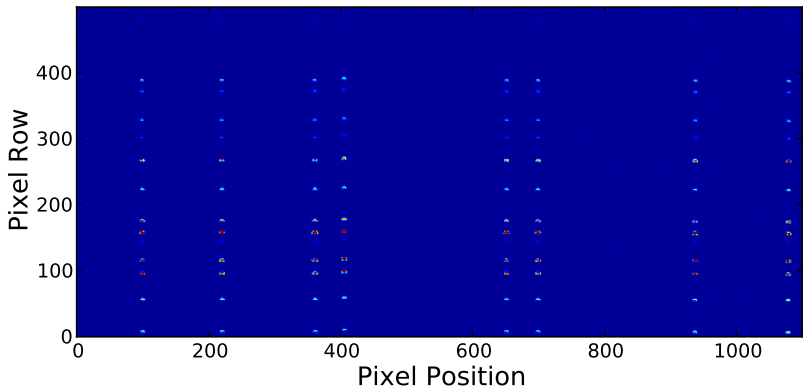

Figure 3.20: Sparsely plugged arc-field image

arcs. Wings are very low signal components so if we use the sparse arcs for our analysis we get negative flux in wing components by nonlinear optimization techniques. This is because the sparse arcs have low signal value for accurate determination of wing parameters.

In the currently implemented optimal extraction technique, the one-dimensional flux profile in a row is modeled with a Gaussian function. Figure 3.21 shows the model to this profile. As the Gaussian function decays abruptly, the model is unable

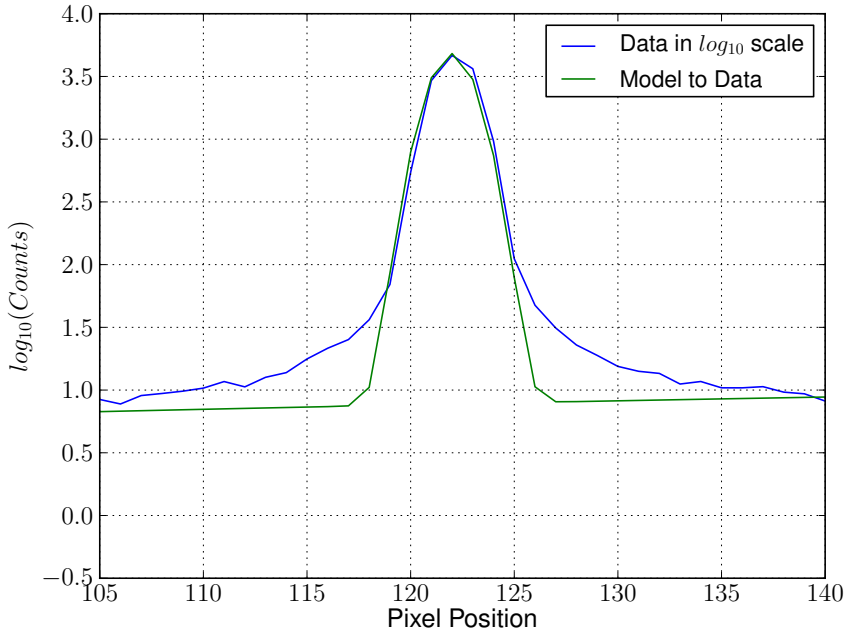

Figure 3.21: Modeling of cross-sectional profile using Gaussian function

to capture the wing component. Hence, we need a slowly decaying function to model the wing component. We use Lorentzian function to model the wing component. Figure 3.22 shows the model for the cross sectional profile which uses Gaussian function to model the core and Lorentzian function to model the wing component. Since Lorentzian is a slowly decaying function the model does not decay abruptly and is able to capture the wings of the one-dimensional profile.

The Lorentzian profile is given as:

$$L(x) = \frac{1}{\pi} \frac{\sigma_w}{(x - x_c)^2 + (\sigma_w)^2}, \tag{3.24}$$

where, x_c is the center of the profile and σ_w is the parameter specifying the width of the profile. We also add a linear background to the model which accounts for the scattered light. We use a linear polynomial to model the background. The model for 1D profile is given as

$$M = aL(x) + (1 - a)G(x) + \text{Linear Background} \tag{3.25}$$

where,

1. $G(x)$ is the normalized 1D Gaussian profile for the core

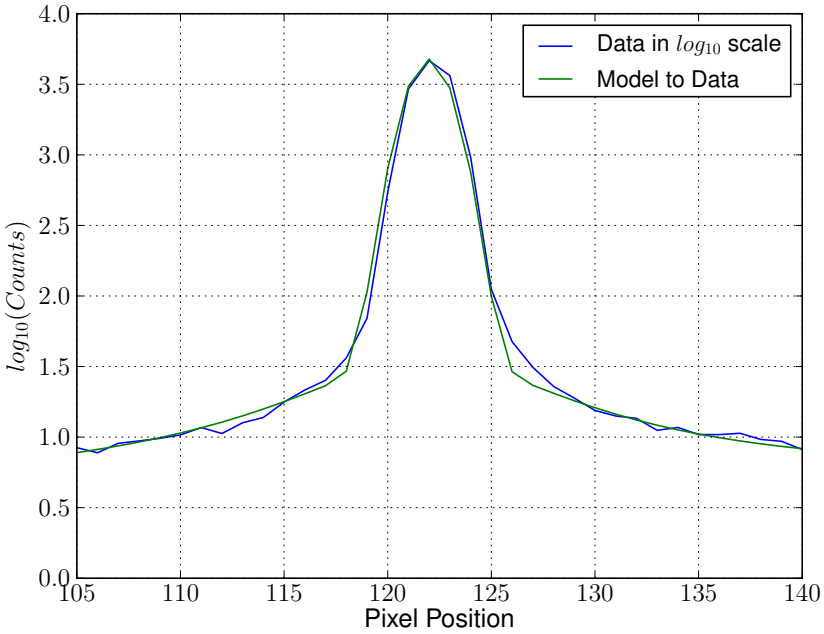

Figure 3.22: Modeling of cross-sectional profile using Gaussian and Lorentzian function

2. $L(x)$ is the normalized Lorentzian profile for the wings

3. a is the fraction of the total flux in the wing component

4. We call this model M as the wing model and it also has a normalized profile.

The parameters of these profiles are:

- Gaussian profile

    1. centroid of the Gaussian profile

    2. width of the Gaussian profile

- Lorentzian profile

    1. width of the wing profile (σ_w)

    2. relative contribution of wing profile (a)

3.4.2 Algorithm to Estimate Parameters of Wing Profile

We have assumed that the 1D profile of a PSF can be defined completely by a Gaussian function for the core and a Lorentzian function for the wings. We fit the model in (3.25) to the data in each row. Since in sparsely plugged images only the fiber is plugged the data in each row are bounded by the central pixel between adjacent fibers. For each row we construct the model **M** by assuming some starting parameters of the model. We fit this model to the data and by techniques of linear optimization estimate the relative flux in the wings. Then we use this relative flux (a) value and by techniques of nonlinear optimization estimate the parameters of the wing component. We construct the model and calculate the error, which is given by

$$E = \sum_i \frac{(D_i - M_i)^2}{N_i^2} \tag{3.26}$$

These two steps are iterated till the error (E) does not reduce any further between two simultaneous executions of these steps.

3.4.3 Results for 1D Lorentzian Profile

The algorithm explained in the previous section is implemented on all the rows of the image. Table 3.2 shows the median value the estimated parameters in different rows. The median width is estimated to be 6 pixels indicating that the one dimensional profile extends 6 pixels on either side from the center. Also, the percentage of flux in wings is around 6% of the total flux.

3.5 Incorporating Wing Profile in 2D PSF

We deproject the 1D profile in two dimensions using the Abel Transform [30] to get a profile for the wing component of the PSF. The estimated width (σ_w) is taken as the width for the deprojected profile in both the x and y direction.

Table 3.2: Estimated Parameters of Lorentzian Profile over the Whole Image

Parameters of Lorentzian Profile	median value of parameter
width	6.0038
fraction of flux in wings	0.0613

The deprojected Lorentzian profile is:

$$L_l^k = \frac{\sigma_w^2}{2\pi} \frac{a}{\left(1 + \frac{(x_l - x_c^k)^2 + (y_l - y_c^k)^2}{\sigma_w^2}\right)^{\frac{3}{2}}},$$

- 2D PSF from fiber k at a particular wavelength is modeled as:

$$M_l^k = a_c v_l^k(t) + L^k f_l,$$

- a_c = 1-a

This is a normalized profile for a 2D PSF after including the wing component.

The System Calibration matrix is now modified to:

$$A_{l,k} = r^k \left(\sum_t c_t a_c v_l^k(t) + c_w L_l^k \right), \tag{3.27}$$

We have to estimate the value of c_t and c_w using (3.20) which give the contribution of Gauss-Hermite as well as deprojected 1D Lorentzian profile.

3.5.1 Results for 2D Lorentzian Profile

In this section we evaluate the performance of Gauss-Hermite model after incorporating a model for wing component on an example image shown in Fig. 3.1. Fig. 3.23 shows the residuals (data - model) of Gauss-Hermite model before incorporating the wing profile and Fig. 3.24 shows the residuals of Gauss-Hermite model after incorporating the wing profile. In Fig. 3.23 we can see the 'halo' regions surrounding the PSF core whereas in Fig. 3.24 after incorporation of the wing profile the undersubtracted regions (halo) are no longer observed and the residuals are close to zero in the wing regions. This indicates that the model is able to capture the wing component.Table 3.3 shows the comparison of Gauss-Hermite model before and after the inclusion of wing profile. For the example image region where we have chosen the χ^2 improves by *28%* and for the whole image the χ^2 improves by *23.5%*. This indicates that to model the PSF accurately we need to include the wing model along with the Gauss-Hermite model. As indicated from Fig 3.24 it also gives a better representation of the PSF as compared to Gauss-Hermite model.

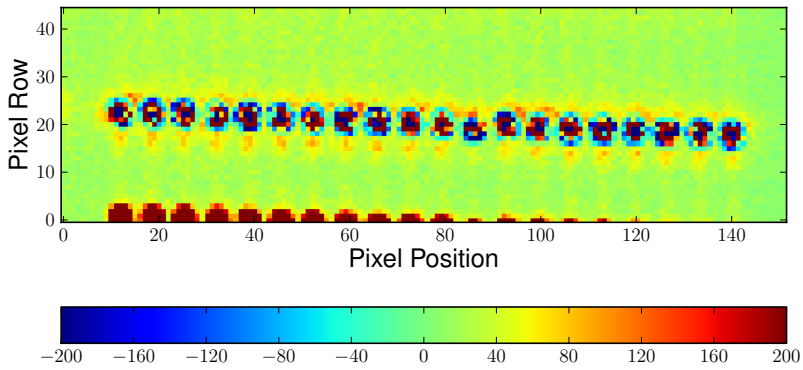

Figure 3.23: Residuals from Gauss-Hermite model

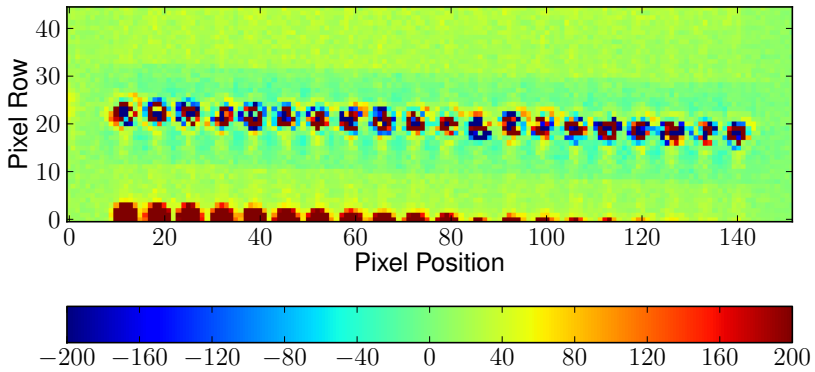

Figure 3.24: Residuals from Gauss-Hermite model after incorporating wings

Table 3.3: Comparison of Performance of Gauss-Hermite Model vs. Wing Model in Terms of Reduced χ^2 (χ^2_r) Value

Model	Gauss-Hermite	Wing Model
example region χ^2_r	28.95	9.77
whole image χ^2_r	24.09	13.65

CHAPTER 4

EXTRACTION

Extraction is defined as the technique of estimation of flux of astronomical objects from CCD images. The aim of this section is to explain extraction of spectra by using the system calibration matrix which we discussed in previous chapters. We also explain the problem associated with deconvolution during extraction of flux from 2D CCD images and the technique undertaken to resolve it. This section also deals with the issue of scattered light and presents an algorithm to remove scattered light from CCD images. At the end we give a quantitative comparison between the 'optimal extraction' technique and our novel technique.

4.1 System Calibration Matrix

We have discussed earlier in Section 1.1 that the 2D PSF is formed by convolution of image of fiber core with the system optics. The shape of the PSF varies across the CCD field of view. We model each PSF as a weighted linear combination of different orders of the Gauss-Hermite functions. In Section 3.2.4 we estimated the coefficients to different Gauss-Hermite orders.

4.1.1 Construction of System Calibration Matrix for Extraction

This section explains the construction of system calibration matrix ($\mathbf{A}$) using the coefficients to Gauss-Hermite functions. The coefficients to Gauss-Hermite function are estimated for all wavelength values which are recorded by the CCD and for all fibers in the CCD. Each PSF is modeled as,

$$v_l^{k,\lambda}(m,n) = \frac{1}{2\pi\sigma^2} H_m\left(\frac{x_l - x_c^k}{\sigma}\right) H_n\left(\frac{y_l - y_c^k}{\sigma}\right) e^{-\frac{1}{2}\left[\frac{(x_l - x_c^k)^2 + (y_l - y_c^k)^2}{\sigma^2}\right]} \tag{4.1}$$

where,

- k represents the fiber
- λ represents the wavelength
- l represents the (i, j) pixel pair
- σ is the value of width of the 1D profile in optimal extraction algorithm. This value is taken from the SDSS database.

The system calibration matrix can be constructed as:

$$A_l^{k,\lambda} = r^{k,\lambda} \sum_t c_t v_l^{k,\lambda}(t) \tag{4.2}$$

where,

- c_t are the Gauss-Hermite coefficients of order t which we have been estimated
- $r^{k,\lambda}$ is the relative fiber throughput of fiber k and wavelength λ

$\mathbf{A}$ is constructed for all wavelength ranges recorded by the CCD. We use h to index all pairs of (k, λ) and l to index all pair of (i, j) pixels. Hence, $\mathbf{A}$ is essentially a two-dimensional matrix. A_l^h defines the noise free count value at pixel l when light of *unit* flux at wavelength λ falls on it from fiber k.

Once $\mathbf{A}$ has been determined we can estimate flux $\mathbf{f}$ using the equation :

$$\mathbf{f} = (\mathbf{A}^T\mathbf{N}\mathbf{A})^{-1}(\mathbf{A}^T\mathbf{N}\mathbf{p}) \tag{4.3}$$

4.1.2 Extraction of Spectra

This section explains the issues related to extraction of spectra. Equation (4.3) gives us the extracted spectra using the system calibration matrix $\mathbf{A}$. This equation not only extracts the spectrum, it also deconvolves the spectral resolution [5]. The instability in deconvolution is seen as "ringing" in the extracted spectrum. Figure 4.1 shows extracted spectrum of a fiber. We are extracting spectra of arc-images and since these images have data only at distinct wavelength we see a peak value at a distinct wavelength in Fig 4.1. Ringing is an undesirable feature in the spectra and our next step is to re-convolve the spectra with its original resolution as the raw data.

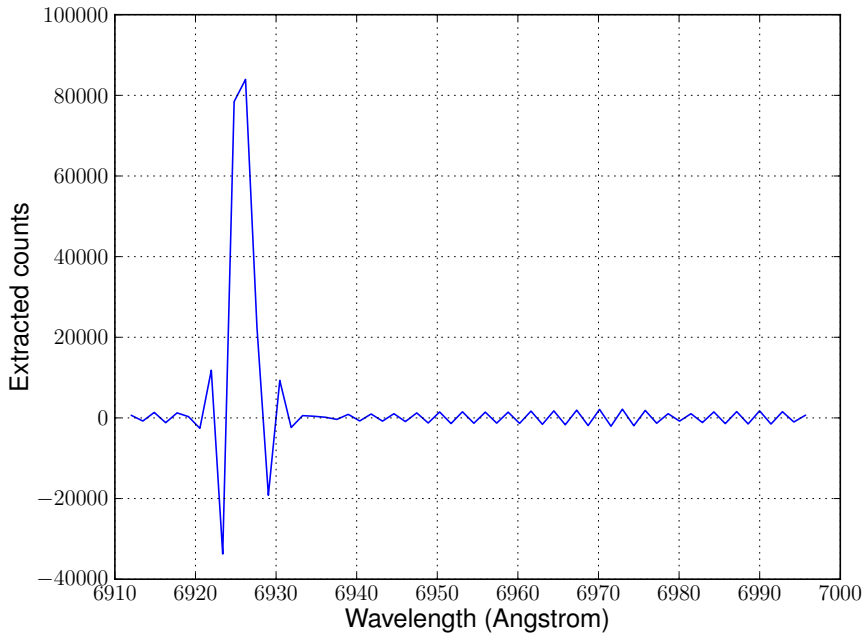

Figure 4.1: Extracted spectra of a fiber, ringing is visible

Consider the inverse covariance matrix (C^{-1}) of the deconvolved spectrum,

$$\mathbf{C}^{-1} = \mathbf{A}^T\mathbf{N}^{-1}\mathbf{A} \tag{4.4}$$

This matrix is symmetric and band diagonal. It is divided into multiple blocks with each block representing correlation between different spectra. Each sub-block along the diagonal shows the coupling between flux samples of the same spectrum. Since these sub-blocks have off-diagonal elements it indicates nonzero correlation between flux samples of the same spectrum. The nonzero elements in the off-diagonal blocks show that we have coupling between spectra of different fibers but this is not important because these spectra are unrelated.

Each k^{th} sub-block, along the diagonal in (4.4) represents the inverse covariance matrix for the flux samples in spectrum k.

We construct an inverse covariance matrix for each spectra. The band diagonal elements of each matrix $\mathbf{C}_k$ is given by the elements of the k^{th} diagonal sub-block.

We can write each k^{th} inverse covariance matrix as

$$\mathbf{C}_k^{-1} = \mathbf{Q}_k^T\mathbf{Q}_k \tag{4.5}$$

Our next step is to diagonalize this matrix to make the flux samples in a spectra statistically independent of each other.

Let us define a normalization vector **s** as,

$$s_{k_l} = \sum_{\tilde{l}} Q_{k_{\tilde{l}\tilde{l}}} \tag{4.6}$$

$$R_{k_{\tilde{l}\tilde{l}}} = s^{-1}_{k_{\tilde{l}}} Q_{k_{\tilde{l}\tilde{l}}} \tag{4.7}$$

Let $\tilde{\mathbf{C}}_k$ be a new diagonal matrix whose entries are given as

$$\tilde{C}^{-1}_{k_{\tilde{l}\tilde{l}}} = s^2_{k_l} \tag{4.8}$$

By construction we have,

$$\tilde{\mathbf{C}_k}^{-1} = \mathbf{R}^{\mathbf{T}}_k \tilde{\mathbf{C}_k}^{-1} \mathbf{R}_k \tag{4.9}$$

and hence,

$$\tilde{\mathbf{C}}_k = \mathbf{R}_k \mathbf{C}_k \mathbf{R}^{\mathbf{T}}_k \tag{4.10}$$

The new covariance matrix $\tilde{\mathbf{C}}_k$ is a diagonal matrix.

Hence the extracted 1D spectrum is

$$\tilde{\mathbf{f}_k} = \mathbf{R}_k \mathbf{f}_k, \tag{4.11}$$

Fig. 4.2 indicates the spectrum obtained after reconvolving the extracted spectra using the resolution matrix $\mathbf{R}_k$. As a result of the reconvolution the ringing has almost reduced to zero. The diagonal covariance matrix, $\tilde{\mathbf{C}}_k$ indicates that the flux samples of a spectrum are statistically independent of each other.

4.2 Scattered Light Subtraction

As we have seen earlier, due to imperfections in the optical assembly the light is scattered and the counts from this scattered light is superimposed on the true count values. We estimate scattered light from the bundle gaps in the CCD image. The bundle gaps are the regions between any two fiber bundles where we do not have

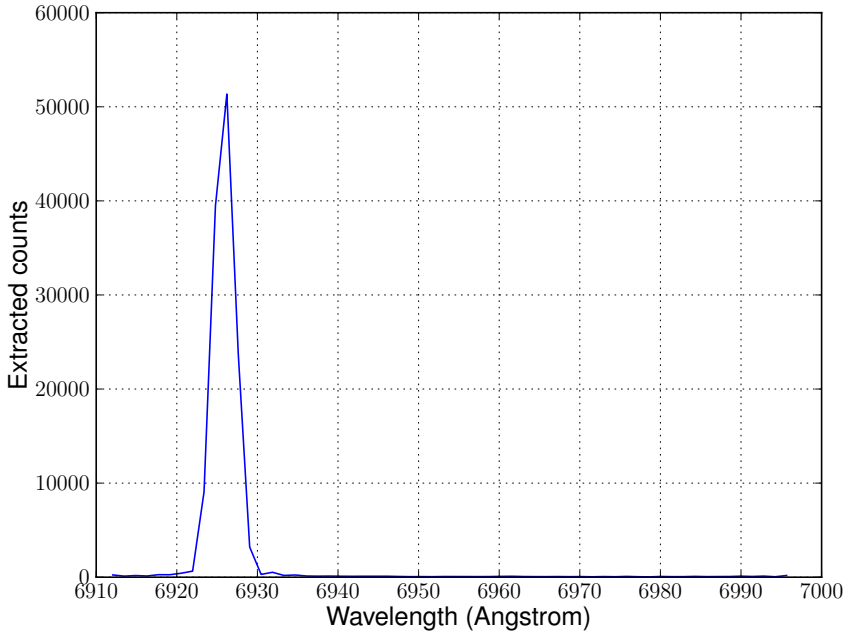

Figure 4.2: Reconvoluted spectra of fiber, ringing is reduced to zero

any optical fiber. Due to the absence of any fiber these regions should ideally have zero count values but due to the presence of scattered light in these regions we can observe count values. Before the extraction of spectra we remove the scattered light component from the calibration images.

4.2.1 Algorithm to Estimate Scattered Light

The aim of this section is to explain the algorithm to estimate the scattered light component in calibration images. Consider a bundle gap between any two fiber bundles. We observe few counts recorded in this region where ideally counts should go to zero. We attribute these counts to scattered light. We fit a bspline curve to the count values in the central pixels of this bundle gap. This is done for all the bundle gaps in the image. Figure 4.3 shows the count values in the central pixels of the rows in a bundle gap. It is difficult to fit these values to any single polynomial function. Hence we use a bspline curve which gives a curve that is an average fit to the count values in a bundle [31]. Figure 4.4 shows the spline fit to the count values in a bundle.

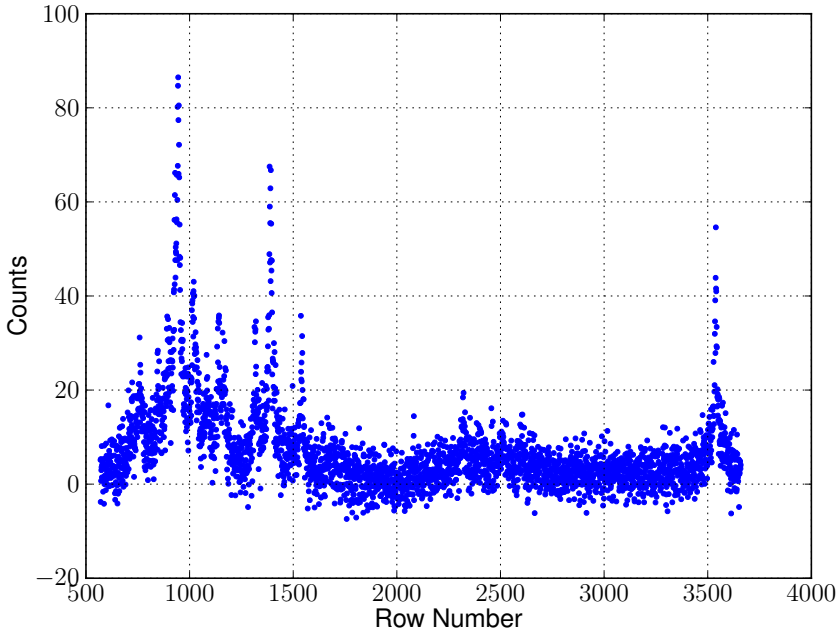

Figure 4.3: Counts recorded due to scattered light in a bundle gap

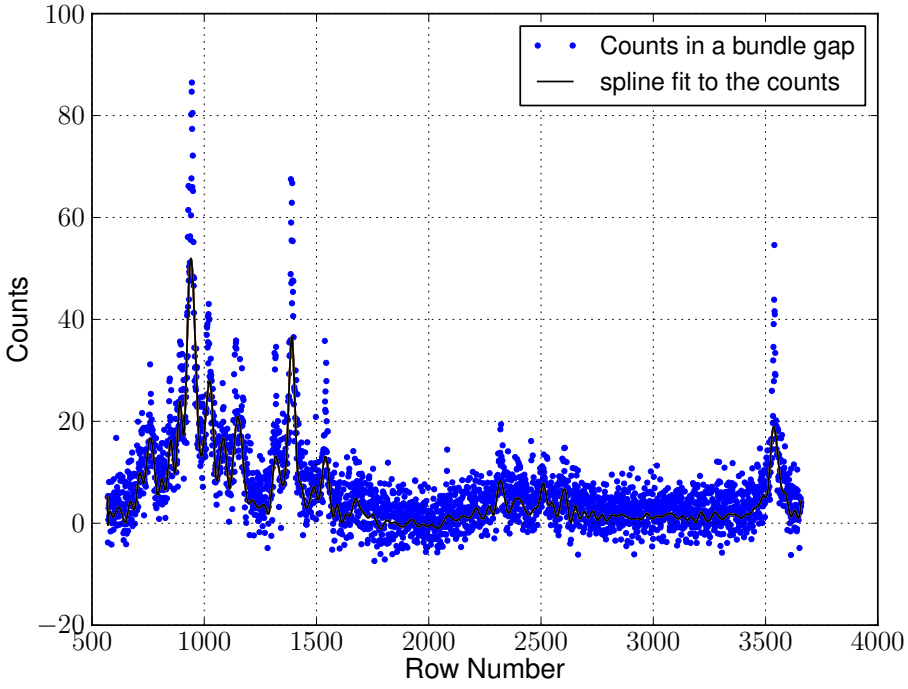

Figure 4.4: Spline fit to counts in a bundle gap

In the next step we estimate the component of scattered light in each pixel of the image. For each row we know the counts recorded due to scattered light in the central pixel of bundle gaps. We fit a bspline curve to each of these value in a row. The spline curve is evaluated at each of the pixel positions in a row to give the counts generated due to scattered light falling on that pixel. This is done for all the rows in the CCD image. As a result, we get a 2D image which gives the counts generated only due to scattered light. This image is subtracted from the data image and the resulting image is used for extraction of spectra from different fibers. Figure 4.5 shows the 2D image where each pixel represents the counts from scattered light. This image will be subtracted from calibration images before the actual extraction.

Figure 4.6 is a section of a bundle gap. It shows the actual counts in the bundle, the fitted counts due to scattered light and the data value after subtracting counts from scattered light. Figure 4.7 shows the same bundle gap after zooming in. We can see the red line which shows the CCD data after subtraction of scattered light. The values after subtraction go to almost zero in these bundle gaps. These bundle gaps are a good indicator of the quality of scattered light subtracted as they themselves do not have any counts from any targeted object. Hence, we expect the counts to go to zero in these regions. From Fig. 4.7 we see that in the bundle gap the count values go to zero indicating that scattered light component has been subtracted.

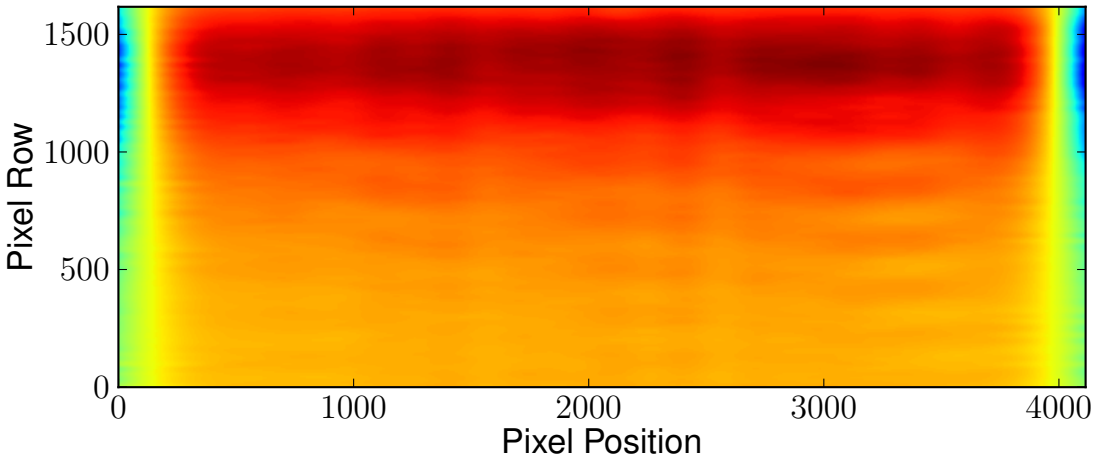

Figure 4.5: 2D image showing scattered light component in each pixel

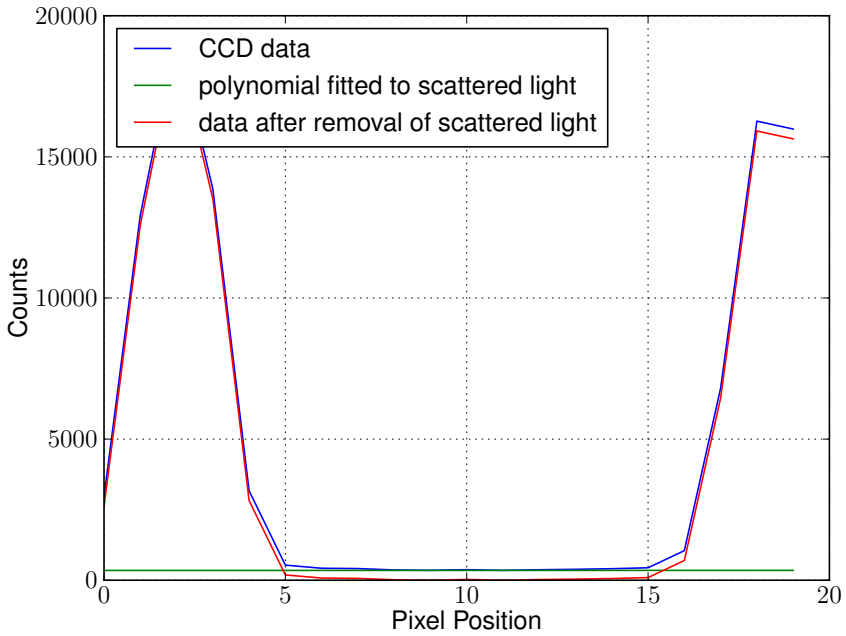

Figure 4.6: Scattered light subtraction in a section of a bundle gap

4.3 Quantitative Comparison Between Row-by-Row and 2D PSF Extraction Technique

In this section we present a quantitative comparison between the standard optimal extraction technique and our 2D PSF extraction technique. We compare the root mean square error (RMSE) of the estimated flux from both the techniques. The RMSE is scaled by the error estimates in each extracted sample

4.3.1 Calculation of RMSE for Row-By-Row Extraction

Using the row-by-row extraction technique as explained in Section 2.2 we extract the spectra from CCD data. In our analysis we extract the spectrum of a bundle at a time. We have used arc-images for extraction and each of the fiber in these images have the same spectrum, which is the spectrum of an arc lamp, used to illuminate these images. Our next step is to estimate a model spectrum of these arc-lamps from all the extracted spectra. In row-by-row extraction we estimate the spectrum of a fiber at each row. The wavelength in each row at which the spectrum is estimated varies with fiber number. This is because of the flexure in the image of the fiber on the CCD, as a result of which light at the same wavelength from different fibers

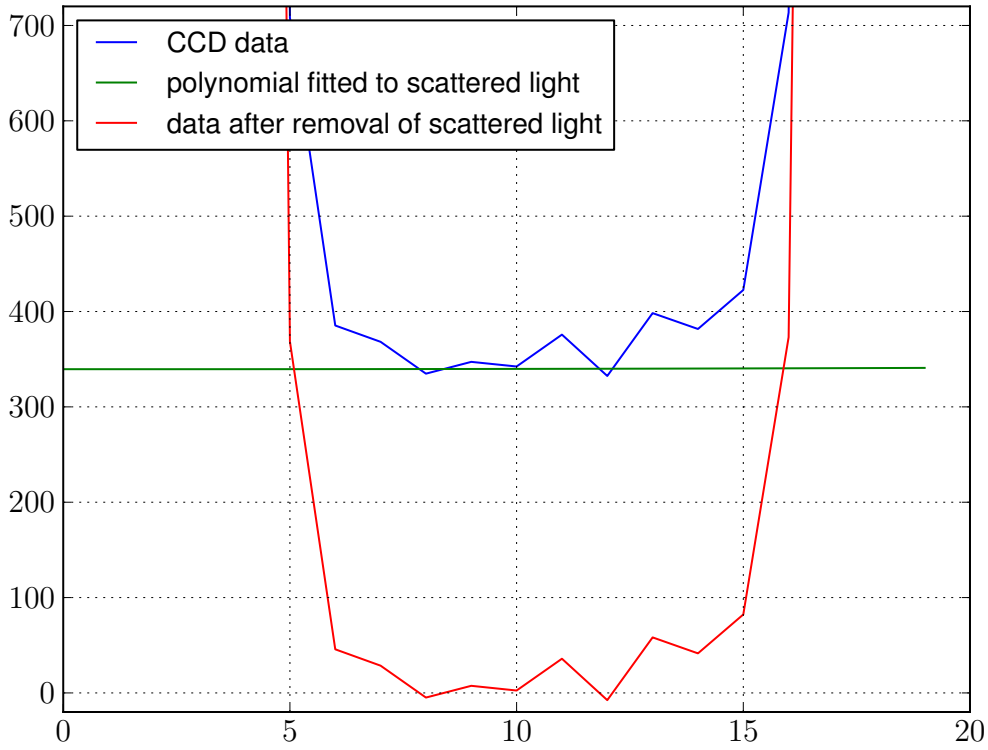

Figure 4.7: Scattered light subtraction after zooming in a section of a bundle gap

falls on different rows. To estimate a common model we fit a bspline curve to the estimated spectrum of all the fibers. The resulting curve is evaluated at wavelength spaced at equal intervals. The interval is given by:

$$\frac{\lambda_{max} - \lambda_{min}}{nrows} \tag{4.12}$$

where,

- nrows: number of rows
- λ_{max}: maximum wavelength in a bundle
- λ_{min}: minimum wavelength in a bundle

For each fiber we subtract the estimated spectrum (by row-by-row technique) from the model spectrum to get residual spectrum. The residual flux is weighted by errors and the RMSE is evaluated.

The errors associated with each of the pixel are given by the square root of the diagonal elements of inverse covariance matrix (C^{-1}).

$$\mathbf{C}^{-1} = \mathbf{A}^{\mathbf{T}}\mathbf{N}^{-1}\mathbf{A} \tag{4.13}$$

4.3.2 2D PSF Extraction

In Section 4.1.2 we discussed 2D PSF extraction of arc-images. In science images, the spectrum of sky is present in all fibers. In these images fibers which carry the spectrum of celestial object, the spectrum of sky is superimposed on them whereas others fibers carry only the spectrum of the sky. The sky spectrum in different fibers is also from one source and is present in all fibers. Similarly the spectra in arc-frames are also from a common arc-lamp and its spectrum is carried by all fibers. So, the spectra in fibers of arc-frames can be assumed to be similar to a sky spectrum. We estimate a common model to the spectra in all the fibers and assume it to be a common model to sky spectrum.

The new calibration matrix used to estimate the common model to the spectra is given as

$$\tilde{A}_{i,j,\lambda} = \sum_{k} A_{i,j,k,\lambda} \tag{4.14}$$

This takes a sum of elements of $\mathbf{A}$ across all fibers at each wavelength to give a new calibration matrix $\tilde{\mathbf{A}}$. This gives us a calibration matrix independent of different fibers. Using $\tilde{\mathbf{A}}$ we estimate the model flux ($\hat{\mathbf{f}}$) for each of the fibers.

$$model\,image = \tilde{\mathbf{A}}\hat{\mathbf{f}} \tag{4.15}$$

We subtract this model image from the data image to give a residual image. We estimate residual flux from the residual image using the extraction explained in Section 4.1.2.

The errors associated with each of the pixel is given by square root of the diagonal elements of the inverse covariance matrix (C^{-1}).

$$\mathbf{C}^{-1} = \mathbf{A}^{\mathbf{T}}\mathbf{N}^{-1}\mathbf{A} \tag{4.16}$$

We remove the ringing effects associated with deconvolution by reconvolving the spectra with the reconvolution matrix $\mathbf{R}$ as given in equation (4.7) and also

diagonalize its inverse covariance matrix using the equation (4.10). We weight the difference between the estimated flux and the model value by the errors and calculate the RMSE as a function of wavelength.

This RMSE tells us the error in the extraction technique when no spectra are observed. So, this represents the noise in the system which will be introduced even when no spectra are observed. We compare this RMSE between both row-by-row and 2D PSF and compare the errors introduced by each technique. We consistently observed 2D PSF extraction technique to perform better than row-by-row extraction technique.

The model spectrum is given in Fig. 4.8. Figure 4.9 shows the comparison between RMSE of the 2D PSF extraction and row-by-row over a bundle. We see that at all wavelengths the RMSE of 2D PSF extraction is less than that of row-by-row extraction. Figure 4.10 gives a comparison of the RMSE of row-by-row and 2D PSF extraction method over a limited range of wavelength in a bundle. Since we have extracted spectra from arc images which are not pointed to the actual sky they record only the spectra of arc-lamps.

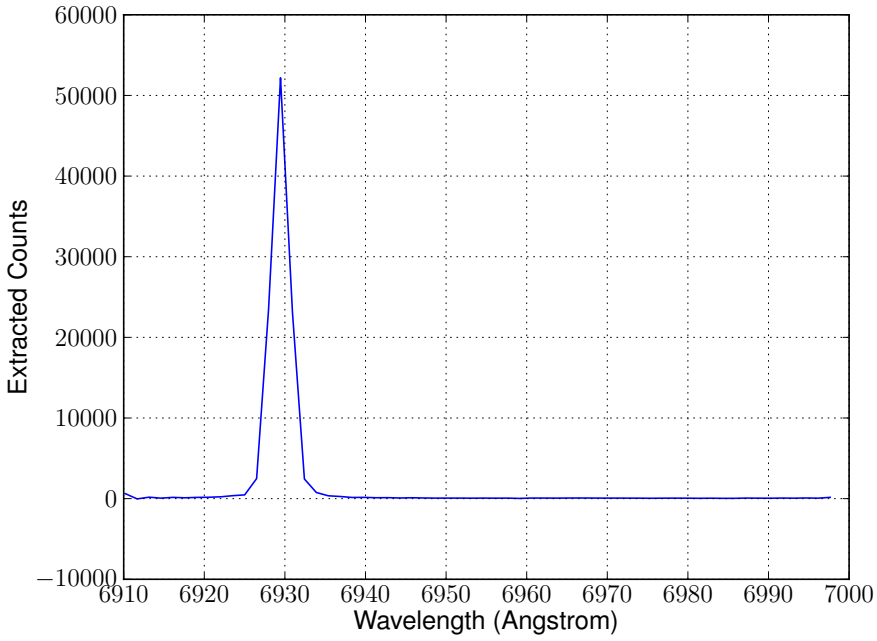

Figure 4.8: Estimated flux

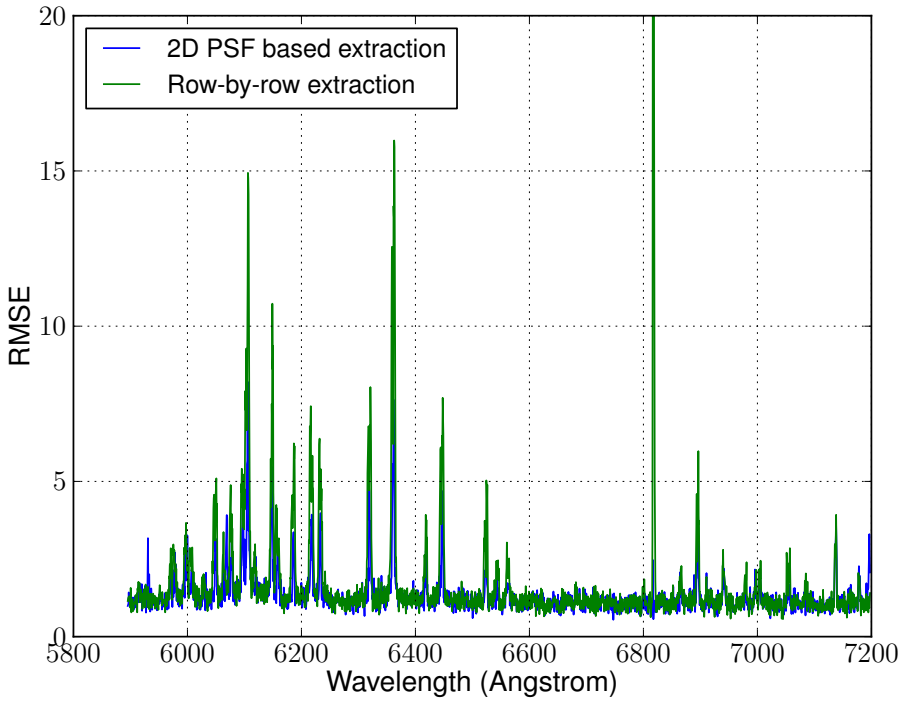

Figure 4.9: RMSE comparison of row-by-row and 2D PSF extraction method

We subtract the model from the extracted spectra and we are only left with noise in the system. We observe that the RMSE (at wavelength 6935$\mathring{A}$ of model spectrum in Fig. 4.8) that is given in Figure 4.10 for a 2D PSF extraction is approximately half of that by row-by-row extraction. From this example image we can infer that for estimation of sky spectrum the error introduced by row-by-row extraction will be twice that of 2D PSF extraction near bright emission lines. As a result the value of residuals of sky-subtraction will be twice in the object spectrum. Faint galaxies have very low signal-to-noise ratio so in the presence of higher sky residuals the estimated spectra of faint galaxies will be noisy and will make the detection of subtle features very difficult. Lower RMSE in 2D PSF extraction will lead to lower sky residuals and the estimated spectra of faint galaxies will be less noisy in comparison to spectra extracted by row-by-row extraction. Figure 4.11 gives the comparison of RMSE of 2D PSF Extraction Method using 4^{th} order Gauss-Hermite model, 6^{th} order Gauss-Hermite model and Wing Model with Gauss-Hermite model for a limited wavelength range. We see that the RMSE of the 6^{th} order and Wing Model decreases in comparison

to the 4^{th} order Gauss-Hermite Model. We have seen earlier that in terms of 2D modeling of raw CCD data also the wing model and 6^{th} order Gauss-Hermite performs better than the 4^{th} order Gauss-Hermite model. Here we compare the Wing model with Gauss-Hermite model in terms of extracted spectra. This is mainly because the Wing model gives a better representation of the 2D PSF as can be seen by the χ^2 improvement of Wing Model in comparison to Gauss-Hermite model. Hence the estimation of $\mathbf{A}$ is improved in Wing Model in comparison to Gauss-Hermite model. This leads to improved estimation of spectra by Wing Model and hence, it has a lower RMSE than the Gauss-Hermite model .

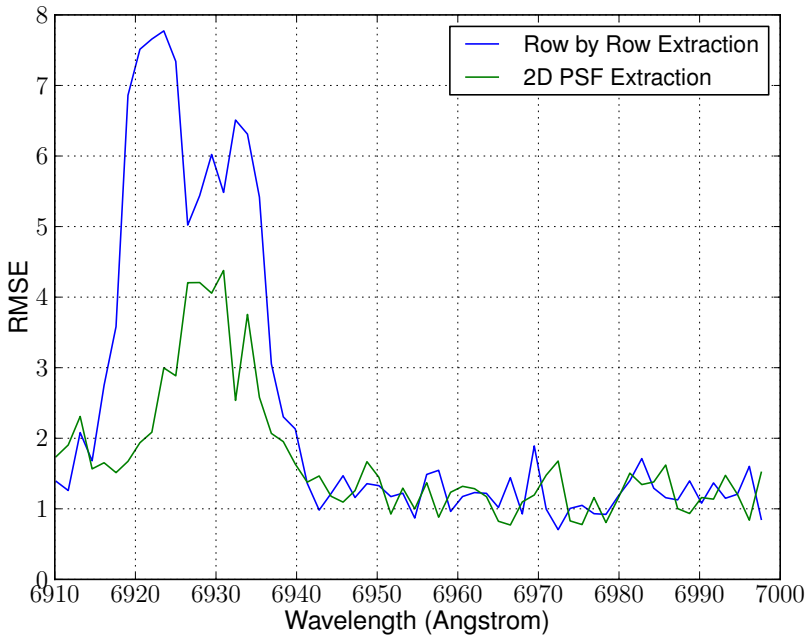

Figure 4.10: RMSE comparison of row-by-row and 2D PSF extraction method for a limited wavelength range

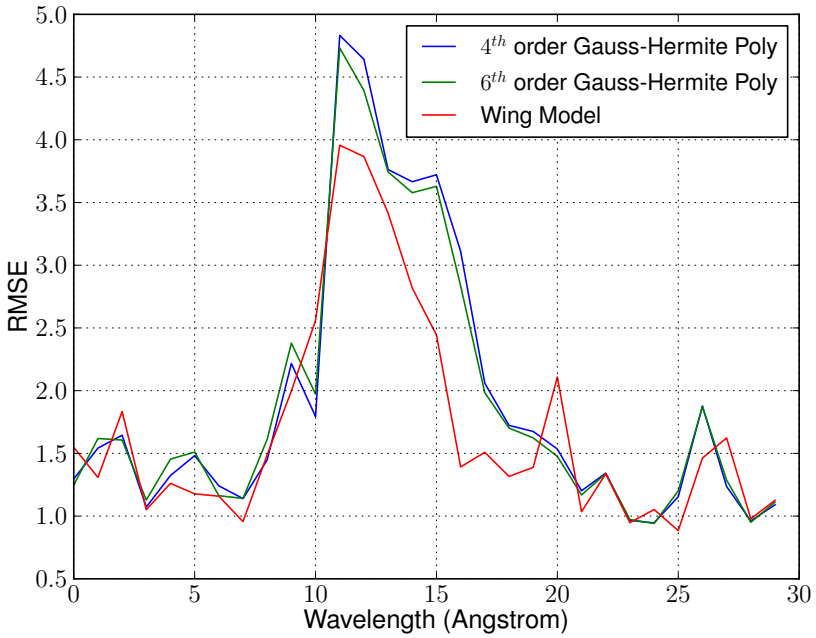

Figure 4.11: RMSE comparison of 2D PSF extraction method using 4^{th} order Gauss-Hermite,6^{th} order Gauss-Hermite and by Wing Model + 4^{th} order Gauss-Hermite

CHAPTER 5

CONCLUSION

Fiber spectroscopy has provided us a great opportunity to record the spectrum of multiple objects together. This advantage has brought with it several drawbacks which must be dealt with. This thesis presented a novel technique to extract the spectrum of objects and also makes an attempt to overcome these drawbacks. We have seen in previous chapters that the performance of our technique is better than the state-of-art techniques. This section aims to summarize the major contribution of our thesis and also the future work which can be undertaken in this direction [21].

5.1 Summary

This thesis presents a novel technique of calibration of astronomical images. In Chapter 3 we presented a model whose parameter **A**, the system calibration matrix has to be estimated. We estimate it elements by modeling the 2D Point Spread Function. Once the system calibration matrix has been estimated the extraction of flux is an inverse problem. The major contributions of this study are:

1. We introduced three models for 2D PSF: Circular Gaussian, Gauss-Hermite and Modified Gauss-Hermite model.

2. We introduced Lorentzian profile to model the wing component of the 2D PSF.

3. We addressed the issue of resolution and covariance in the extracted spectra, and presented a method that established optimal properties in both these regards.

The performance comparison of the models using the χ^2 tests show that the Gauss-Hermite model performs better by 40% in comparison to the circular Gaussian profile, because it is able to capture the skewness and ellipticity in data. We also introduced a modified form of Gauss-Hermite model called modified Gauss-Hermite function.

The performance of this model decreased in comparison to Gauss-Hermite model by *12.21*%. We also subtracted the component of scattered light from 2D CCD images. We also modeled the wing component in the 2D PSF by using a Lorentzian profile. As a result of incorporating the wing profile the performance of the Gauss-Hermite model improved by *23.52*% in comparison to only modeling the core of the PSF. At the end we presented a quantitative comparison between the row-by-row extraction and 2D PSF extraction technique. We saw the RMSE of 2D PSF was significantly lower than that of row-by-row extraction.

5.2 Future Work

This research is an alternative to the existing calibration techniques in the field of astronomy. Problems associated with these techniques have been discussed in Chapter 2. This research provides a novel technique of modeling the PSF. We have presented various models to do so and also compared our models qualitatively with the existing techniques. Although we have covered all aspects of modeling of PSF there are certain research areas which can be undertaken after modeling of PSF is done. The major research directions in this area are :

1. Extraction of Flat and Science data
2. Analysis of tunable laser data as 'best case calibration' example
3. Faster implementation

5.2.1 Extraction of Flat and Science Data

Our technique has focussed mainly on extraction of arc-images but this technique can be applied to other images too like the object and flat image frames.

5.2.2 Analysis of Tunable Laser Data as 'Best Case Calibration' Example

The discharge lamps used to construct the calibration images do not have the same intensity at all wavelengths. As a result, the pixel count values vary at different wavelengths. Also for a few discrete wavelengths the discharge lamps emit light at

wavelengths close to each other because of which the PSFs at these wavelengths overlap with each other. To estimate the parameters of a PSF at a wavelength accurately, we have to model it in isolation without any interference from PSFs at other wavelength. Blending leads to inaccurate determination of weights to Gauss-Hermite polynomials. Also, in Fig.3.9 we see that from wavelength range 7500 to 8200 Angstroms we have to mask the coefficient value because they overshoot either because of low count values or blending between adjacent PSFs. As a result we do not get weights at well sampled in wavelength range. Tunable lasers can be used to overcome these problems. These lasers generate light of equal intensity and at evenly spaced wavelengths. The tunable laser test data are available for BOSS spectrograph, and they may be used to establish the performance of the algorithms under optimal calibration-data conditions. [32]

5.2.3 Faster Implementation

To estimate the spectra we use (4.3) where the square matrix ($\mathbf{A^T N^{-1} A}$) which is inverted, is of size $N_{\text{spectra}} \times N_{\text{samples per spectrum}}$. For SDSS-III the number of spectra are 500 and number of samples per spectrum is approximately 4000. As a result, this square matrix with each size being 2 million. With the present computational capability available it is not possible to store this matrix in dense form. Since this is a sparse matrix we can utilize the sparsity of the matrix to store this matrix. Even with sparse matrix implementation the execution time of the extraction algorithm is high. At present we extract the spectrum of one bundle (20 fibers) at a time. We need to implement better storage methods and faster execution methods for extraction algorithm. We can also implement high performance parallel computing to extract all bundles together.

REFERENCES

[1] D. Schlegel, M. White, and D. Eisenstein, "The Baryon Oscillation Spectroscopic Survey: Precision measurements of the absolute cosmic distance scale," *Arxiv preprint arXiv:0902.4680*, 2009.

[2] H. Baba, N. Yasuda, S. Ichikawa *et al.*, "Adass xi, ed. da bohlender, d. durand, & th handley," in *ASP Conf. Ser*, vol. 281, 2002, p. 298.

[3] A.Bolton, S. Bailey, J. Brownstein, P.Pandey, D.Schlegel, and Y.Shu, in *ADASS XXI*, vol. TBD, 2012.

[4] M. Jarvis, P. Schechter, and B. Jain, "Telescope optics and weak lensing: PSF patterns due to low order aberrations," *ArXiv e-prints*, Oct. 2008.

[5] A. Bolton and D. Schlegel, "Spectro-Perfectionism: An algorithmic framework for photon noise-limited extraction of optical fiber spectroscopy," *Arxiv preprint arXiv:0911.2689*, 2009.

[6] A. Davenhall, "The fibre spectroscopy cookbook," *Ref: http://docs.jach.hawaii.edu/star/sc14.ps*.

[7] D. Gray, *The observation and analysis of stellar photospheres*. Cambridge Univ Pr, 2005.

[8] D. Schlegel, M. White, and D. Eisenstein, "Astro2010: The astronomy and astrophysics decadal survey," *Science White Papers*, vol. 314, 2009.

[9] A. Bolton, S. Burles, D. Schlegel, D. Eisenstein, and J. Brinkmann, "Sloan digital sky survey spectroscopic lens search. i. discovery of intermediate-redshift star-forming galaxies behind foreground luminous red galaxies," *The Astronomical Journal*, vol. 127, p. 1860, 2004.

[10] V. Wild and P. Hewett, "Evidence for dust reddening in damped lyα absorbers identified through ca ii (h&k) absorption," *Monthly Notices of the Royal Astronomical Society: Letters*, vol. 361, no. 1, pp. L30–L34, 2005.

[11] K. Horne, "An optimal extraction algorithm for CCD spectroscopy," *Publications of the Astronomical Society of the Pacific*, vol. 98, pp. 609–617, 1986.

[12] R. Bacon, Y. Copin, G. Monnet, B. Miller, J. Allington-Smith, M. Bureau, C. Marcella Carollo, R. Davies, E. Emsellem, H. Kuntschner *et al.*, "The sauron project–i. the panoramic integral-field spectrograph," *Monthly Notices of the Royal Astronomical Society*, vol. 326, no. 1, pp. 23–35, 2001.

[13] T. R. Marsh, "The extraction of highly distorted spectra," *PASP*, vol. 101, pp. 1032–1037, Nov. 1989.

[14] N. Piskunov and J. Valenti, "New algorithms for reducing cross-dispersed echelle spectra," *Astronomy and Astrophysics*, vol. 385, no. 3, pp. 1095–1106, 2002.

[15] J. G. Robertson, "Optimal extraction of single-object spectra from observations with two-dimensional detectors," *PASP*, vol. 98, pp. 1220–1231, Nov. 1986.

[16] C. W. Stubbs and J. L. Tonry, "Toward 1% photometry: End-to-end calibration of astronomical telescopes and detectors," *APJ*, vol. 646, pp. 1436–1444, Aug. 2006.

[17] M. Cushing, W. Vacca, and J. Rayner, "Spextool: A spectral extraction package for spex, a 0.8-5.5 micron cross-dispersed spectrograph," *Publications of the Astronomical Society of the Pacific*, vol. 116, no. 818, pp. 362–376, 2004.

[18] A. Bolton and S. Burles, "An integral-field spectroscopic strong lens survey," *New Journal of Physics*, vol. 9, p. 443, 2007.

[19] W. Dixon, "Callfuse version 3: A data reduction pipeline for the far ultraviolet spectroscopic explorer," DTIC Document, Tech. Rep., 2007.

[20] B. Cui, Z. Ye, and Z. Bai, "The extraction algorithm for lamost two-dimensional spectrum image," *Acta Astronomica Sinica*, vol. 49, pp. 327–338, 2008.

[21] R. Sharp and M. N. Birchall, "Optimal extraction of fibre optic spectroscopy," *PASA*, vol. 27, pp. 91–103, Mar. 2010.

[22] C. Sandin, T. Becker, M. Roth, J. Gerssen, A. Monreal-Ibero, P. B{öhm, and P. Weilbacher, "p3d: A general data-reduction tool for fiber-fed integral-field spectrographs," *Arxiv preprint arXiv:1002.4406*, 2010.

[23] P. C. Hewett, M. J. Irwin, P. Bunclark, M. T. Bridgeland, E. J. Kibblewhite, X. T. He, and M. G. Smith, "Automated analysis of objective-prism spectra. I - Quasar detection," *MNRAS*, vol. 213, pp. 971–989, Apr. 1985.

[24] S. Howell, *Handbook of CCD astronomy*. Cambridge Univ Pr, 2006, vol. 5.

[25] S. Kay, *Fundamentals of Statistical Signal Processing, Volume I: Estimation Theory*. Prentice Hall, 1993, vol. 1.

[26] C. Bishop and SpringerLink, *Pattern recognition and machine learning*. Springer New York, 2006, vol. 4.

[27] E. Hecht, *Optics 2nd edition by Eugene Hecht Reading, MA: Addison-Wesley Publishing Company, 1987*, vol. 1, 1987.

[28] J. Jackson and R. Fox, "Classical electrodynamics," *American Journal of Physics*, vol. 67, p. 841, 1999.

[29] M. Rice, *Digital communications: A discrete-time approach*. Prentice Hall, 2009.

[30] J. Binney and S. Tremaine, *Galactic dynamics*. Princeton Univ Pr, 1988.

[31] S. McKinley and M. Levine, "Cubic spline interpolation," *Ref: http://online. redwoods. cc. ca. us/instruct/darnold/laproj/Fall98/SkyMeg/proj. pdf.*

[32] C. Stubbs and J. Tonry, "Toward 1% photometry: End-to-end calibration of astronomical telescopes and detectors," *The Astrophysical Journal*, vol. 646, p. 1436, 2006.